

Left-Right Symmetry Breaking and Gravitational Waves : A Tale of Two Phase Transitions

Z. A. Borboruah^a U. A. Yajnik^a

^a*Department of Physics, Indian Institute of Technology Bombay, Mumbai 400076, India*

E-mail: zafri123@iitb.ac.in, yajnik@iitb.ac.in

ABSTRACT: We study possible ways gravitational waves (GW) get sourced in a theory with minimal left-right symmetry breaking. The breaking of discrete parity combined with the limitation of light cone in the early Universe leads to interesting variants on the standard classification of phase transitions. If local effective potential signals second order phase transition (SOPT) or a cross over, breaking of discrete parity in conjunction with finiteness of the causal horizon leads to a *causal horizon limited* second order phase transition, which results in domain walls separating left-like and right-like domains. On the other hand for the case of usual first order phase transition (FOPT), we get the usual signal from spontaneously created bubbles, but also, as we argue from a lingering late time domain wall structure separating the two types of vacua. Thus the putative SOPT also gives rise to GW, testable via experiments such as IPTA, and DECIGO and LISA. Further, the traditional FOPT case gives rise to two distinct peaks in the spectrum of GW, verifiable for the low symmetry breaking scales $10^4 - 10^6$ GeV, but beyond the reach of currently planned experiments for a high scale $\sim 10^{10}$ GeV. Finally we point out that a version of the left-right symmetric model which separates parity breaking from gauge symmetry breaking is also subject to domain wall formation and amenable to GW observations.

Contents

1	Introduction	2
2	Minimal Left-Right Symmetric Model	4
2.1	Potential	4
2.2	Effective Potential	6
2.3	Two kinds of phase transitions	7
3	The causal horizon limited Second order Phase Transition (SOPT)	9
3.1	GW from Domain Wall Decay	9
3.2	Benchmark values	11
4	Numerical Simulation	14
4.1	Equation of Motion	14
4.2	Simulation Setup	15
4.2.1	Initial Field Configuration	16
4.3	Scaling Regime	18
4.4	Gravitational Wave Spectrum	20
5	Gravitational waves from First-order Phase Transition	21
5.1	Bubble Collision	24
5.2	Sound Waves	24
5.3	MHD Turbulence	25
5.4	Degenerate field FOPT	25
6	Dissociating Parity breaking from LR Symmetry Breaking	26
7	Conclusion	27
A	Appendix	29
A.1	Rescaling the Field Equation	29
A.2	Calculation of Gravitational Waves	30
A.2.1	Discretizing Equation of Motion	32
A.2.2	Periodic Boundary Condition:	33
A.2.3	Stability Condition:	34

1 Introduction

The detection of gravitational waves (GWs) [1] has opened a new window into the unknown of the Universe. Originating from the linearized theory of general relativity [2], GWs are a new independent source of information about cosmic events. Also, since gravitation is the weakest force in nature, gravitons are believed to decouple from the rest of the forces and matter as early as the Planck scale itself, meaning they can convey information from the very dawn of the Universe.

The early Universe GW sources include not only astronomical objects, but cosmological events like inflation, phase transitions, etc. Throughout time, GWs from all such events superimpose to create what's called a *stochastic background of GWs*, which is believed to be homogeneous, isotropic, unpolarized with an amplitude following a Gaussian distribution [3]. Several current and future experiments are aimed at detecting this background, directly via interferometers [4, 5] or through indirect methods like Pulsar Timing Arrays (PTAs) [6]. This GW background can be a good alternative probe for high and ultra high energy phenomena including those arising from grand unified theories (GUTs) and other particle physics theories beyond the Standard Model (SM).

One such high energy theory is the *Left-Right Symmetric Model* (LRSM), especially since it accommodates massive neutrinos with well defined gauge charges for the new right handed neutrino states. Based on the gauge group $SU(2)_L \otimes SU(2)_R \otimes U(1)_{B-L}$, this model is fully symmetric between right and left chiral states at high temperature in the early Universe when the thermal ground state does not break symmetry spontaneously. As such why low energy physics is governed by $SU(2)_L \times U(1)_Y$ is unknown. Early proposal to rectify this situation was made in [7, 8] by dissociating spontaneous breaking of the so called *D-parity* from the breaking of right-handed gauge symmetry, by invoking an extra scalar beyond the basic LRSM particle content.

But as we will discuss later in this paper, this scenario also cannot avoid domain walls and will also contribute to the GW background. Conventionally LRSM is spontaneously broken down to SM through additional Higgs particles, for example using scalar $SU(2)$ doublets or triplets in the supersymmetric (SUSY) [9, 10] and Non-SUSY [11–19] contexts. A *minimal left-right symmetric model* (MLRSM) with scalar triplets has garnered much attention because it can implement the seesaw mechanism and can be embedded in a $SO(10)$ grand unified theory (GUT) nicely [20–24]. LRSM has been studied extensively in view of the present and future colliders [25–32] but LHC has detected no evidence of it up to $\mathcal{O}(10 \text{ TeV})$. Therefore the GW background presents the exciting possibility providing the first hints of this theory, especially if originating at significantly higher energies, thus complementing the role of future colliders.

The breaking of discrete symmetry $L \leftrightarrow R$ which is generically exact in left-right symmetric models leads to formation of domain walls (DW) in the early Universe. Domain walls are massive topological defects created when a discrete symmetry is broken [33, 34]. They separate two regions of distinct degenerate vacua of the theory. This is a problem for standard cosmology, as stable domain walls come to dominate the energy density of the Universe at later times [35] and conflict with structure formation and Big Bang

Nucleosynthesis (BBN). Therefore, they must be transient [36–41]. This can be achieved by making one of the vacua slightly lower in energy so that the domain walls move under the vacuum pressure. Eventually violent collisions between DW causes their annihilation returning the Universe to a homogeneous state after entropic equilibrium is reached.

While it is usual to identify phase transitions in gauge theories as First Order (FOPT), Second order (SOPT) or crossover, the left-right symmetric models present a peculiar situation, due to the presence of causal horizons in the Big Bang Universe. While the effective potential may signal a second-order phase transition, the correlation lengths remain limited by the causal horizon, thus evading the the divergence of length scales characteristic of the SOPT. In fact the situation is further complicated by the fact that the two degenerate vacua are characterised by vacuum expectation values (VEV's) of two distinct fields, so that in causally disconnected regions distinct fields, eg., $SU(2)_L$ triplet having VEV on one side of the wall (right-like vacuum), while $SU(2)_R$ triplet acquiring a VEV (left-like vacuum) on the other side of the wall. This is also the case when the local effective potential signals a cross over phase transition. It is seems best to characterise this as "causal horizon limited SOPT", to be abbreviated as CHL-SOPT. The eventual state resulting from such a phase transition will be a network of domain walls, with the domains alternately enclosing left-like and right-like vacua. This is also the case when the local effective potential signals a cross over phase transition.

Likewise, even the putative FOPT is fundamentally modified in that the spontaneous formation of bubbles of true vacuum could either lead to bubbles of left-like vacuum or right-like vacuum. When these bubbles grow and encounter each other, the collision can result in a larger bubble, provided the interiors contain the same type of vacuum. On the other hand if one bubble contains left-like while the other contains right-like vacuum then the result is a stable left-right domain wall of the type discussed in [42, 43]. The situation is depicted in Fig. 1. The eventual result of such a phase transition will also be a network of domain walls enclosing distinct types of vacua, making it look similar to SOPT of a different scale. We refer to this as the Degenerate Field FOPT.

Gravitational waves from first-order phase transition [44–50] and more specifically from MLRSM [51] have been studied extensively which we will discuss in section 5. The several contributions to the GW resulting from SOPT have been identified to be [52–54] from 1) evolution of the initial quantum fluctuations of the fields and 2) late time evolution of massive Domain Walls. At late times, the contribution from the former becomes insignificant compared to the contribution from the latter. This paper will consider the CHL-SOPT case, and calculate the energy spectrum of the gravitational waves produced. Our approach parallels the methods used in [52–54] but with the difference that we consider the late time evolution of domain walls after the Ginzburg temperature has been reached in the context of LRSM. For the Degenerate Field FOPT case we determine the double peak spectrum for models with symmetry breaking scales $10^4 - 10^6$ GeV and $\sim 10^{10}$ GeV and discuss the possibility of their verifiability.

The arrangement of this paper is as follows: in the next section, we will describe the MLRSM with triplets and the loop corrected temperature dependent effective potential. We determine benchmark points in the parameter space which result in first-order or second-

order phase transitions. In a subsection we emphasise the cosmology of these two kinds of phase transitions, identifying CHL-SOPT and Degenerate Field FOPT. In Section 3, we discuss GWs from CHL-SOPT followed by a section describing the numerical methods used to simulate the decaying domain walls. In Section 5, we discuss GWs for the Degenerate Field FOPT case, identifying the two peak feature. In sec. 6 we show that the LRSM scenario of [7, 8] also results in characteristic GW background.

2 Minimal Left-Right Symmetric Model

The MLRSM [55–62] is an appealing extension of the SM which naturally accords gauge charges to the right-handed neutrino states which are generically needed to provide masses to neutrinos. It is based on the gauge group,

$$\mathcal{G}_{LR} \equiv SU(2)_L \times SU(2)_R \times U(1)_{B-L} \times SU(3)_C \quad (2.1)$$

where the electric charge is defined as

$$Q = T_{3L} + T_{3R} + \frac{B-L}{2}. \quad (2.2)$$

Under this left-right symmetric gauge group, the usual quarks and leptons transform as

$$\begin{aligned} q_L = \begin{pmatrix} u_L \\ d_L \end{pmatrix} &\equiv [2, 1, 1/3, 3], & q_R = \begin{pmatrix} u_R \\ d_R \end{pmatrix} &\equiv [1, 2, 1/3, 3], \\ \ell_L = \begin{pmatrix} \nu_L \\ e_L \end{pmatrix} &\equiv [2, 1, -1, 1], & \ell_R = \begin{pmatrix} \nu_R \\ e_R \end{pmatrix} &\equiv [1, 2, -1, 1]. \end{aligned}$$

The Higgs sector may vary in LRSM. We will focus on the minimal Higgs sector containing the triplets and the bidoublet [63], $\Delta_L(1, 0, 2, 0)$, $\Delta_R(0, 1, 2, 0)$, $\phi(1/2, 1/2^*, 0, 0)$. They can be represented in the matrix form,

$$\phi = \begin{pmatrix} \phi_1^0 & \phi_1^+ \\ \phi_2^- & \phi_2^0 \end{pmatrix}, \quad \Delta_L = \begin{pmatrix} \frac{1}{\sqrt{2}}\delta_L^+ & \delta_L^{++} \\ \delta_L^0 & -\frac{1}{\sqrt{2}}\delta_L^+ \end{pmatrix}, \quad \Delta_R = \begin{pmatrix} \frac{1}{\sqrt{2}}\delta_R^+ & \delta_R^{++} \\ \delta_R^0 & -\frac{1}{\sqrt{2}}\delta_R^+ \end{pmatrix} \quad (2.3)$$

so that they transform as

$$SU(2)_L \times SU(2)_R : \phi \rightarrow U_L \phi U_R^\dagger, \quad \Delta_L \rightarrow U_L \Delta_L U_L^\dagger, \quad \Delta_R \rightarrow U_R \Delta_R U_R^\dagger \quad (2.4)$$

$$U(1)_{B-L} : \phi \rightarrow \phi, \quad \Delta_L \rightarrow e^{i2\theta} \Delta_L, \quad \Delta_R \rightarrow e^{i2\theta} \Delta_R \quad (2.5)$$

for general symmetry transformations: $U_L \in SU(2)_L$, $U_R \in SU(2)_R$, and $e^{i\theta} \in U(1)_{B-L}$.

2.1 Potential

The tree-level standard scalar potential of the LRSM with triplets is given by,

$$V_0 = V_\phi + V_\Delta + V_{\phi\Delta} \quad (2.6)$$

where

$$\begin{aligned}
V_\phi &= -\mu_1^2 \text{Tr} [\phi^\dagger \phi] - \mu_2^2 \left(\text{Tr} [\tilde{\phi} \phi^\dagger] + \text{Tr} [\tilde{\phi}^\dagger \phi] \right) + \lambda_1 \text{Tr} [\phi^\dagger \phi]^2 + \lambda_2 \left(\text{Tr} [\tilde{\phi} \phi^\dagger]^2 + \text{Tr} [\tilde{\phi}^\dagger \phi]^2 \right) \\
&\quad + \lambda_3 \text{Tr} [\tilde{\phi} \phi^\dagger] \text{Tr} [\tilde{\phi}^\dagger \phi] + \lambda_4 \text{Tr} [\phi^\dagger \phi] \left(\text{Tr} [\tilde{\phi} \phi^\dagger] + \text{Tr} [\tilde{\phi}^\dagger \phi] \right), \\
V_\Delta &= -\mu_3^2 \left(\text{Tr} [\Delta_L \Delta_L^\dagger] + \text{Tr} [\Delta_R \Delta_R^\dagger] \right) + \rho_1 \left(\text{Tr} [\Delta_L \Delta_L^\dagger]^2 + \text{Tr} [\Delta_R \Delta_R^\dagger]^2 \right) \\
&\quad + \rho_2 \left(\text{Tr} [\Delta_L \Delta_L] \text{Tr} [\Delta_L^\dagger \Delta_L^\dagger] + \text{Tr} [\Delta_R \Delta_R] \text{Tr} [\Delta_R^\dagger \Delta_R^\dagger] \right) + \rho_3 \text{Tr} [\Delta_L \Delta_L^\dagger] \text{Tr} [\Delta_R \Delta_R^\dagger] \\
&\quad + \rho_4 \left(\text{Tr} [\Delta_L \Delta_L] \text{Tr} [\Delta_R^\dagger \Delta_R^\dagger] + \text{Tr} [\Delta_L^\dagger \Delta_L^\dagger] \text{Tr} [\Delta_R \Delta_R] \right), \\
V_{\phi\Delta} &= \alpha_1 \text{Tr} [\phi^\dagger \phi] \left(\text{Tr} [\Delta_L \Delta_L^\dagger] + \text{Tr} [\Delta_R \Delta_R^\dagger] \right) + \alpha_3 \left(\text{Tr} [\phi \phi^\dagger \Delta_L \Delta_L^\dagger] + \text{Tr} [\phi^\dagger \phi \Delta_R \Delta_R^\dagger] \right) \\
&\quad + \alpha_2 \left(\text{Tr} [\Delta_L \Delta_L^\dagger] \text{Tr} [\tilde{\phi} \phi^\dagger] + \text{Tr} [\Delta_R \Delta_R^\dagger] \text{Tr} [\tilde{\phi}^\dagger \phi] + \text{h.c.} \right) \\
&\quad + \beta_1 \left(\text{Tr} [\phi \Delta_R \phi^\dagger \Delta_L^\dagger] + \text{Tr} [\phi^\dagger \Delta_L \phi \Delta_R^\dagger] \right) + \beta_2 \left(\text{Tr} [\tilde{\phi} \Delta_R \phi^\dagger \Delta_L^\dagger] + \text{Tr} [\tilde{\phi}^\dagger \Delta_L \phi \Delta_R^\dagger] \right) \\
&\quad + \beta_3 \left(\text{Tr} [\phi \Delta_R \tilde{\phi}^\dagger \Delta_L^\dagger] + \text{Tr} [\phi^\dagger \Delta_L \tilde{\phi} \Delta_R^\dagger] \right) \tag{2.7}
\end{aligned}$$

where $\tilde{\phi} = \sigma_2 \phi^* \sigma_2$. All the couplings are assumed to be real for simplicity. The vacuum expectation values (VEVs) of the Higgs fields that gives the correct breakdown of LR symmetry are as follows,

$$\langle \phi \rangle = \frac{1}{\sqrt{2}} \begin{pmatrix} \kappa_1 & 0 \\ 0 & \kappa_2 e^{i\theta_2} \end{pmatrix}, \quad \langle \Delta_L \rangle = \frac{1}{\sqrt{2}} \begin{pmatrix} 0 & 0 \\ v_L e^{i\theta_L} & 0 \end{pmatrix}, \quad \langle \Delta_R \rangle = \frac{1}{\sqrt{2}} \begin{pmatrix} 0 & 0 \\ v_R & 0 \end{pmatrix} \tag{2.8}$$

The bidoublet VEV's provide the electroweak scale,

$$\sqrt{\kappa_1^2 + \kappa_2^2} = v = 246 \text{ GeV} \tag{2.9}$$

and the parameter $\beta = \arctan \kappa_2 / \kappa_1$ captures the ratio of the VEV's. The minimisation conditions on the potential, with respect to the four VEV's leads to a relationship between v_L and v_R through a see-saw-like formula,

$$\beta_1 \kappa_1 \kappa_2 \cos(\theta_2 - \theta_L) + \beta_2 \kappa_1^2 \cos \theta_L + \beta_3 \kappa_2^2 \cos(2\theta_2 - \theta_L) = (2\rho_1 - \rho_3) v_L v_R \tag{2.10}$$

It is customary to set $\beta_{1,2,3} = 0$ so that the strong condition of this see-saw can be circumvented, v_L can be chosen 0 while v_R can be assigned phenomenologically desirable large value. Additionally θ_2 and θ_L may be set to 0 for simplicity.

We shall use the VEV's from SM and expected phenomenology as the inputs in the minimization conditions, in which case the parameters $\mu_{1,2,3}^2$ get determined as follows.

$$\begin{aligned}
\mu_1^2 &= \lambda_1 (\kappa_1^2 + \kappa_2^2) + 2\kappa_1 \kappa_2 \lambda_4 + \frac{1}{2} v_R^2 \alpha_1 - \frac{\alpha_3}{2} \frac{v_R^2 \kappa_2^2}{\kappa_1^2 - \kappa_2^2} \\
\mu_2^2 &= (2\lambda_2 + \lambda_3) \kappa_1 \kappa_2 + \frac{\lambda_4}{2} (\kappa_1^2 + \kappa_2^2) + \frac{\alpha_2}{2} v_R^2 + \frac{\alpha_3}{4} \frac{v_R^2 \kappa_1 \kappa_2}{\kappa_1^2 - \kappa_2^2} \\
\mu_3^2 &= \rho_1 v_R^2 + \frac{1}{2} \alpha_1 (\kappa_1^2 + \kappa_2^2) + 2\alpha_2 \kappa_1 \kappa_2 + \frac{1}{2} \alpha_3 \kappa_2^2 \tag{2.11}
\end{aligned}$$

An important point which has not received due attention in the literature is that the see-saw-like relation equally well implies a possible large value for v_L and $v_R \approx 0$ due to

the left-right symmetry of the model. While low energy phenomenology has preferred the $v_L \approx 0$ solution, this will not persist at high temperature in the early Universe. Indeed we expect gauge symmetry restoration at high temperature [? ? ?], a scale T_c above which the thermal ground state has no non-zero VEV's. When the Universe cools it must choose between the left-like vacuum with $v_L \neq 0$ or right-like vacuum with $v_R \neq 0$. As already introduced in Sec. 1, this leads to intricate possibilities for the nature of the phase transition, as we further discuss in Sec. 2.3

2.2 Effective Potential

From low energy phenomenology we are interested in scenarios where the $SU(2)_R$ breaking scale is much higher than electroweak symmetry breaking $v_R \gg \kappa_1, \kappa_2$. It turns out that it is sufficient to focus on large δ_R^0 values in field space, compared to the remaining neutral fields r_1^0, r_2^0 and δ_L^0 [51]. However in the context of the early Universe the alternative possibility of v_L being large, while ignoring v_R also arises. Hence we retain the two contributions in the tree level potential from δ_R^0 , and δ_L^0

$$V_0^{total}(r, l) = V_0(r) + V_0(l) \quad (2.12)$$

where $r = \delta_R^0/\sqrt{2}$ and $l = \delta_L^0/\sqrt{2}$, and V_0 are both identical functional forms of their arguments,

$$V_0(r) \approx \frac{\rho_1}{4} (r^2 - \eta^2)^2 \quad (2.13)$$

where $\eta = \sqrt{\mu_3^2/\rho_1}$. Note that it is sufficient to consider only the first quadrant $r > 0, l > 0$ of the $r - l$ plane. Indeed due to the see-saw type condition, where $r \rightarrow 0, l \rightarrow v_L \neq 0$ and vice versa. As such we expect domain walls, separating regions of left-like vacuum $l \neq 0, r = 0$ and $l = 0, r \neq 0$ with the wall constituting a transition region where one VEV goes to zero and the other turns on.

Let us focus on generalising the functional form (2.13) of the potential to the case of non-zero temperature. The temperature-dependent effective potential is given by [51],

$$V_{\text{eff}}(r, T) = V_0(r) + V_{\text{CW}}(r) + V_{\text{FT}}(r, T) + V_{\text{D}}(r, T) \quad (2.14)$$

where

$$V_{\text{CW}}(r) = \frac{1}{64\pi^2} \left[\sum_i m_i^4(r) \left(\log \frac{m_i^2(r)}{\mu^2} - \frac{3}{2} \right) + 6m_{W_R}^4(r) \left(\log \frac{m_{W_R}^2(r)}{\mu^2} - \frac{5}{6} \right) \right. \\ \left. + 3m_{Z_R}^4(r) \left(\log \frac{m_{Z_R}^2(r)}{\mu^2} - \frac{5}{6} \right) - 6m_{\nu_R}^4(r) \left(\log \frac{m_{\nu_R}^2(r)}{\mu^2} - \frac{3}{2} \right) \right] \quad (2.15)$$

is the Coleman-Weinberg correction to the tree potential and,

$$V_{\text{FT}}(r, T) = \frac{T^4}{2\pi^2} \left[\sum_i J_{\text{B}} \left(\frac{m_i^2(r)}{T^2} \right) + 6J_{\text{B}} \left(\frac{m_{W_R}^2(r)}{T^2} \right) + 3J_{\text{B}} \left(\frac{m_{Z_R}^2(r)}{T^2} \right) - 6J_{\text{F}} \left(\frac{m_{\nu_R}^2(r)}{T^2} \right) \right] \quad (2.16)$$

is the temperature correction from finite temperature field theory, where $J_{B/F}$ are integrals for bosons/fermions given by,

$$J_{B/F}(r^2) = \int_0^\infty dx x^2 \log\left(1 \mp e^{-\sqrt{x^2+r^2}}\right) \quad (2.17)$$

The mass terms $m_i, m_{W_R}, m_{Z_R}, m_{\nu_R}$ are the field (r) dependent scalar, gauge and fermion masses [51]. The μ in (2.15) is the renormalization scale which we can conveniently assume to be equal to v_R . The last term includes the Daisy diagrams for higher loop corrections,

$$V_D(r, T) = -\frac{T}{12\pi} \sum_j [M_j^3(r) - m_j^3(r)] \quad (2.18)$$

where M_j are given by eigenvalues of the matrices $\mathcal{M}_j + \Pi_j$ where \mathcal{M}_j are mass matrices of bosons and fermions and Π_j are thermal self energies [51]. The summation of j includes all the bosons and fermions of the theory. Finally,

$$V_{eff}^{total}(r, l, T) = V_{eff}(r, T) + V_{eff}(l, T) \quad (2.19)$$

2.3 Two kinds of phase transitions

The finite temperature effective potential V_{eff} in Eq. (2.19) demonstrates a phase transition from the parity symmetric $v_R = v_L = 0$ state at high temperature to the parity violating $v_R \neq v_L = 0$ state at low temperature. The transition occurs at a critical temperature ($T = T_c$), and can be of two types: first-order or second-order, depending on whether or not the potential V_{eff} has two degenerate global minima at T_c . However for the left-right case this classification needs to be modified for two different reasons : finite causal horizon in the early Universe [64][65], and the fact that there are two fields Δ_L and Δ_R obeying a potential symmetric under $\Delta_L \leftrightarrow \Delta_R$. We may thus identify two possibilities :

- **Causal horizon limited SOPT** : SOPT is characterised by fluctuation length $\xi = 1/m_r = (\sqrt{2\rho_1\eta})^{-1}$, the inverse mass of the Higgs degree of freedom r in Eq. (2.13). However, the phase transition can be considered to have ended only after the temperature drops below the Ginzburg temperature corresponding to the correlation length ξ_G

$$\xi_G \simeq \frac{1}{2\rho_1\eta} \quad (2.20)$$

This is determined from the condition that

$$\xi_G^3 \Delta_c V_{eff} = T_G \quad (2.21)$$

which defines T_G implicitly, where $\Delta_c V_{eff}$ is the difference between free energy density in the two phases. In the early Universe this length is further restricted by the condition that the correlation length cannot be diverging faster than the speed of light, which then implies that the relevant correlation length is

$$\xi_{causal} = \left(\frac{M_{Pl}}{\sqrt{\mathcal{N}}m_r^2 T_c^2}\right)^{1/3} \quad (2.22)$$

The implication of these considerations is that as the correlation length reaches its maximum value, uncorrelated regions with either $v_L \neq 0$ or $v_R \neq 0$ are allowed to develop, with domain walls forming between them. This is unusual for a SOPT, but is true in the present theory. Thus ξ_{causal} can be considered to provide the scale of domain sizes just below the temperature T_G .

- **Degenerate fields FOPT** : In this case, while the true vacuum bubbles form spontaneously, they can contain either $v_L \neq 0$ or $v_R \neq 0$. In addition, as sketched in Fig. 1, after the merger of same type of vacua, there will arise a residual network of frustrated domain walls at a larger length scale.

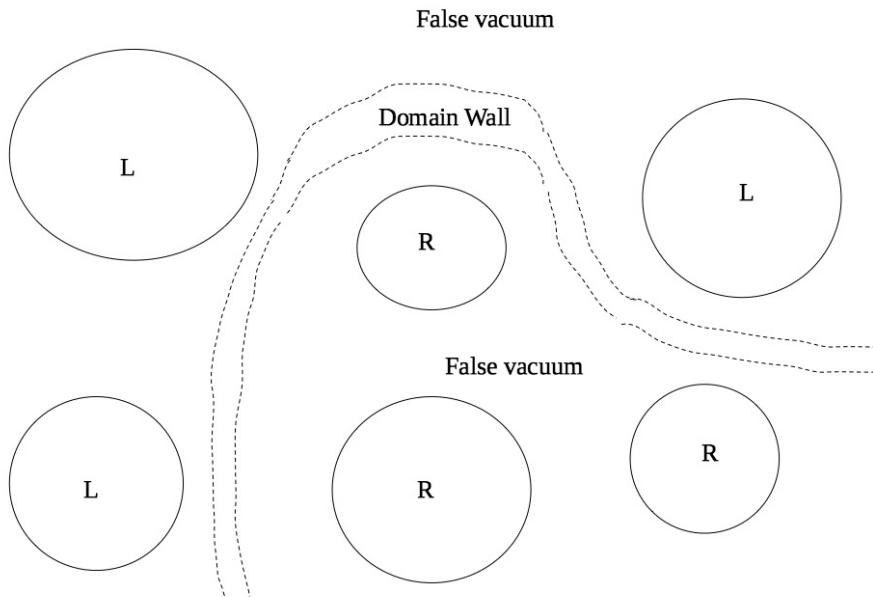


Figure 1: Cartoon explaining the emergence of residual domain walls after FOPT in the case of two degenerate fields such as in the left-right symmetric model. The symmetric false vacuum can be destabilised by spontaneous formation of bubbles of either L type vacuum with $v_L = 0$ and $v_R \neq 0$ or R type with $v_R = 0$ and $v_L \neq 0$. The domain wall sketched with dotted lines eventually emerges as the bubbles of same type true vacua merge to form large homogeneous domains.

Using the tunnelling probability formula in terms of the bounce solution, one introduces a time scale : inverse duration of a phase transition (see Eq. (5.6)) β . So long as $\beta \gtrsim H$, sufficient number of bubbles will be formed that they can percolate[35, 66]. However the percolation can be either among the left-like or the right-like phases. Where the two percolated regions meet, there is a domain wall, until the whole Universe is filled with a frustrated network of domain walls. In the absence of any other scales, it is reasonable to assume that over scales greater than the causal horizon, the next near neighbour domain can randomly be in the same or the other vacuum. This can lead to a frustrated network of scale larger than the causal horizon by a factor $O(1)$

though not much larger. The particle physics model therefore needs to contain a mechanism for a slow disintegration of these residual walls in order to not conflict with late cosmology.

The subsequent evolution of these residual domain walls depends on the bias between the two types of approximately degenerate vacua. Finally, the false domains will shrink out of existence according to the bias, producing GWs from the late time evolution of the decay of these domain walls. Thus in addition to the spontaneous bubbles of the usual FOPT we get a contribution from the CHL-SOPT type evolution of disintegrating DW. Since the two epochs are well separated in time we can calculate each contribution individually.

We shall discuss the causal horizon limited SOPT in Section 5 and degenerate fields FOPT in section 3. As we shall see, the contributions from the pure FOPT and the CHL-SOPT are well separated in frequency space, allowing piece together the result for the Degenerate Field FOPT case from the two results.

3 The causal horizon limited Second order Phase Transition (SOPT)

3.1 GW from Domain Wall Decay

For the potential in Eq. (2.13), with two degenerate minima at $r = \pm\eta$, one can find a static solution of the equation of motion with boundary conditions that the two minima are realized at the extremities, i.e. $r(x = \pm\infty) = \pm\eta$, of the form,

$$r(x) = \eta \tanh\left(\frac{1}{2} \frac{x}{\delta_{\text{wall}}}\right) \quad (3.1)$$

where x is the spatial co-ordinate. This represents a domain wall extended along $x = 0$ plane. δ_{wall} is the DW width, approximately equal to the inverse of the mass of the field r ,

$$\delta_{\text{wall}} \sim m_r^{-1} = \left(\sqrt{2\rho_1}\eta\right)^{-1} \quad (3.2)$$

Another important parameter of a domain wall is the tension, given by,

$$\sigma_{\text{wall}} = \int_{-\infty}^{\infty} dx \rho_r = \frac{2}{3} m_r \eta^2 \quad (3.3)$$

where $\rho_r = \frac{1}{2} |\nabla r|^2 + V_0(r)$ is the static energy density of the field. These two parameters basically characterise a domain wall.

The evolution of the domain wall is determined by the Klein-Gordon equation. As discussed in section 2.3, in case of a second-order phase transition, *frustrated* domain walls are produced which move under the vacuum pressure difference between the true and the false vacua. Following [52], we introduce a small bias in the tree potential in Eq. (2.13) which breaks the degeneracy of the two minima of the form,

$$V_{\text{bias}} = \epsilon \eta r \left(\frac{r^2}{3} - \eta^2\right) \quad (3.4)$$

where ϵ is a very small number. This term introduces an energy difference between the two minima $\delta V = 4\epsilon\eta^4/3$, which in turn exerts a vacuum pressure on the domain wall $p_V \sim \delta V$. The pressure difference should be large enough to make the walls disappear before DWs start dominating the energy density of the Universe. The decay time is given by,

$$t_{\text{dec}} = \frac{1}{2} \sqrt{\frac{\rho_1}{2}} (\epsilon\eta)^{-1} \quad (3.5)$$

However, due to the requirement that both vacua percolate, the energy difference can't be arbitrarily large. The ratio of the percolation probabilities is given by $p_+/p_- \simeq e^{-4\delta V/\rho_1\eta^4}$ [34], which gives an upper bound on the bias $\epsilon \leq -\frac{3}{16}\rho_1 \log[(p_+/p_-)_{\text{min}}]$. In 3D cubic lattice, if the probability of attaining a vacuum p_{\pm} is greater than a critical value $p_c = 0.311$, then infinite clusters of the vacuum can form [67]. Assuming $p_+ = 0.311$ and $p_- = 1 - 0.311 = 0.689$ we get,

$$\epsilon \leq 0.15\rho_1 \quad (3.6)$$

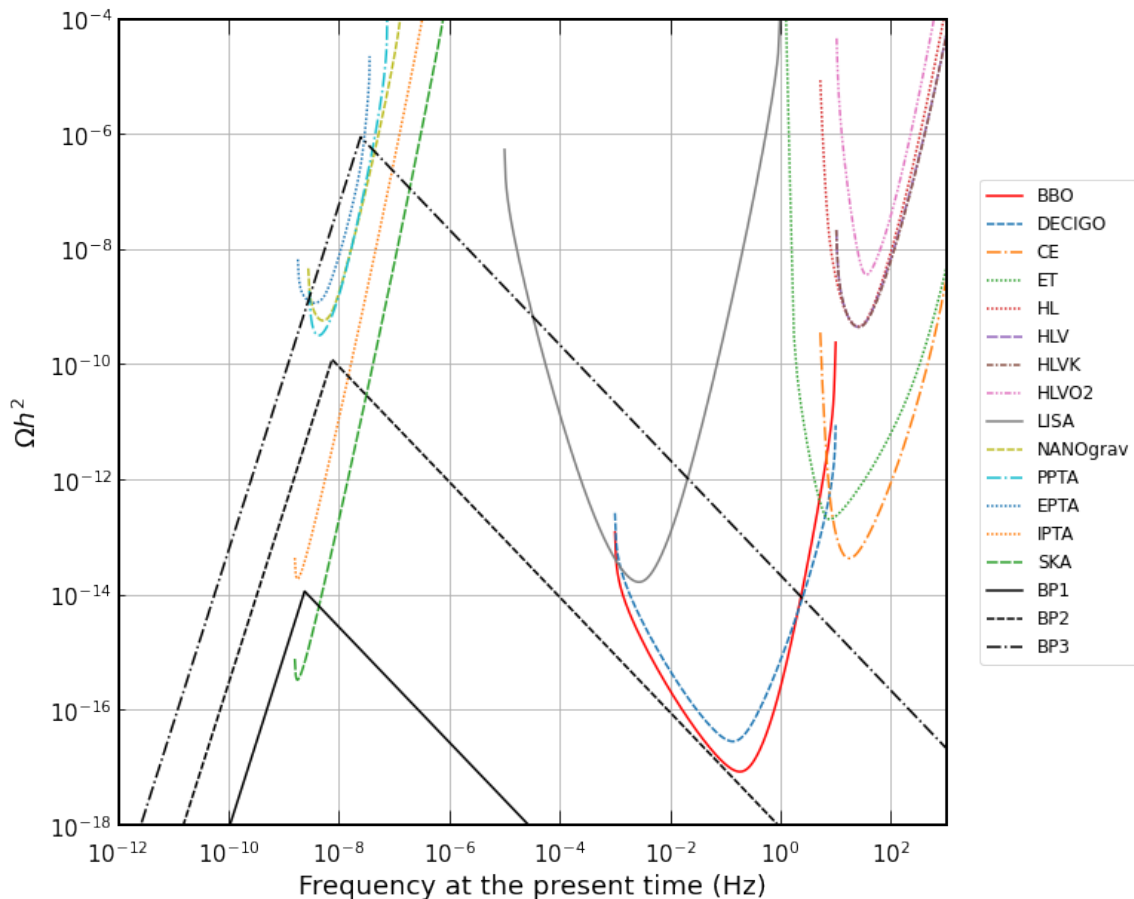


Figure 2: GW spectrum as seen today, from crumbling DWs for BP1, BP2, BP3 with $v_R = 10^4, 10^5, 10^6$ GeV respectively and the bias, $\epsilon = 2 \times 10^{-26}$, in comparison to *power-law-integrated-sensitivities* of different experiments.

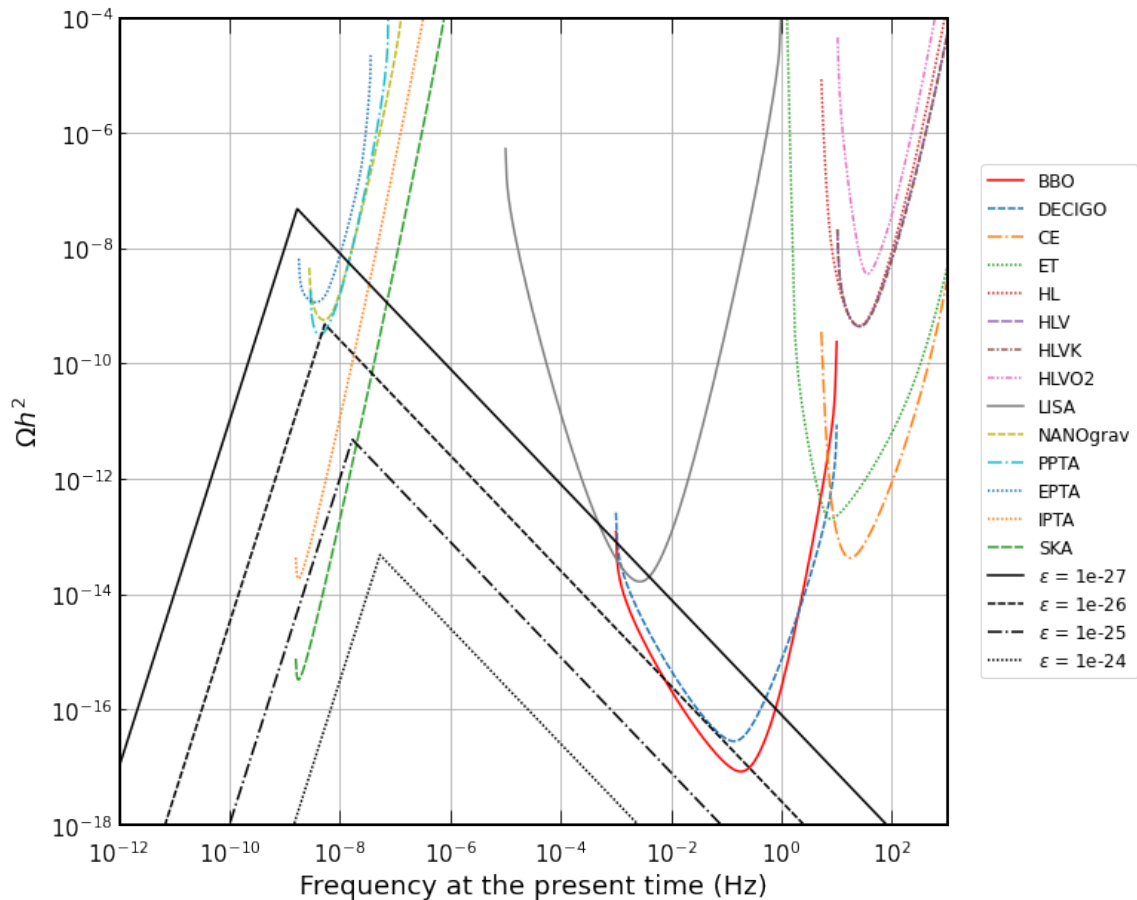


Figure 3: GW spectrum for BP2 with $\eta = 10^5$ GeV and bias, $\epsilon = 10^{-27}, 10^{-26}, 10^{-25}, 10^{-24}$. The smaller the bias, the more the amplitude but we can't have an arbitrarily small bias since that will make the domain walls enter the scaling regime.

On the other hand, requirements for the well-known *scaling solution* gives another bound [68],

$$\epsilon < 4.7 \times (\rho_1 g_*)^{1/2} \frac{\eta}{M_P} \quad (3.7)$$

where g_* is the number of relativistic degrees of freedom at transition temperature T_c and M_P is the Planck mass. Requiring that the walls decay before they dominate the energy density, we get a lower bound on the bias [68],

$$\epsilon > \frac{16\pi}{9} \rho_1 \left(\frac{\eta}{M_P} \right)^2 \quad (3.8)$$

3.2 Benchmark values

For evaluating the potential given in Eq. (2.14) and see what type of phase transitions take place, we use *Mathematica*. LRSM is very constrained in terms of realization and parameters. In the triplet model, we set the β_i s to be 0 to obtain observable gauge and Higgs bosons [63]. We consider the parameter space for our model as in [51]:

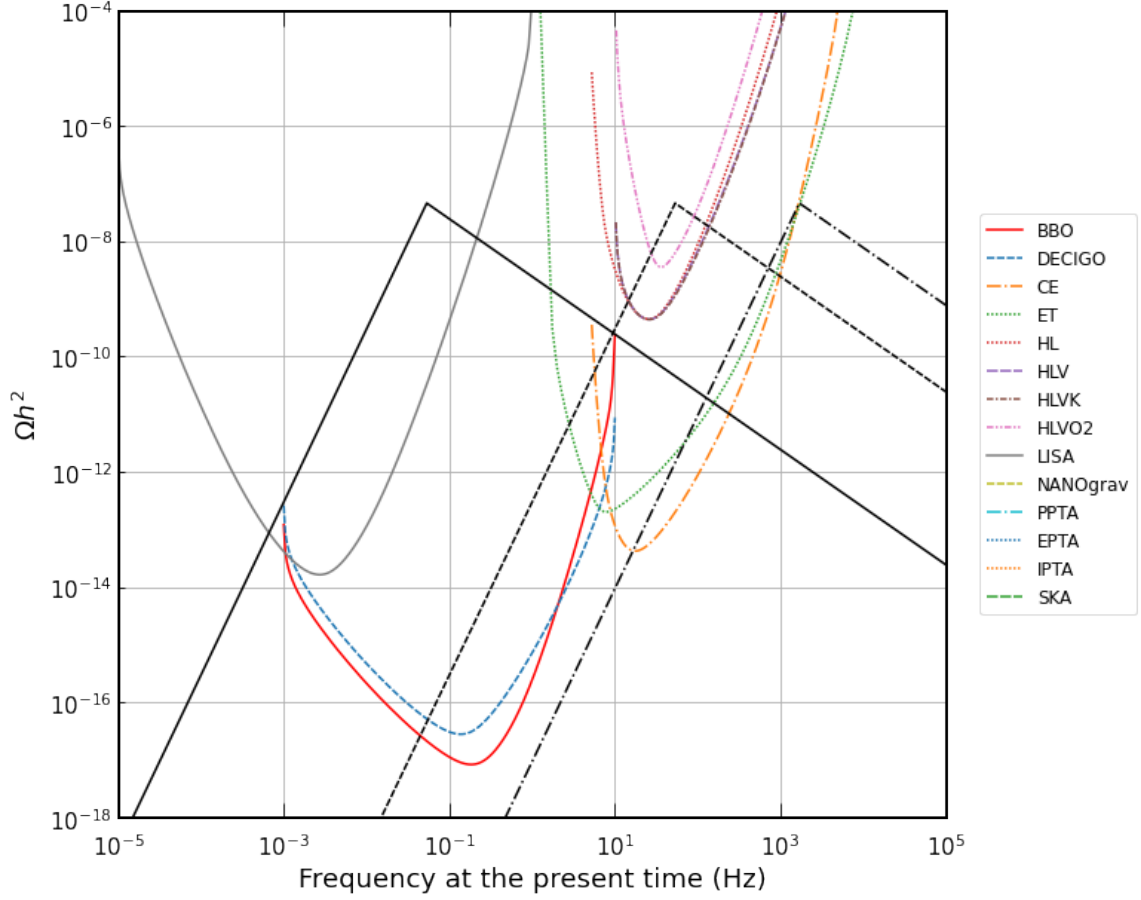


Figure 4: GW spectrum (in black) for $(\eta, \epsilon) = (10^{10}\text{GeV}, 10^{-17})$ (solid), $(\eta, \epsilon) = (10^{12}\text{GeV}, 10^{-13})$ (dashed) and $(\eta, \epsilon) = (10^{13}\text{GeV}, 10^{-11})$ (dot-dashed). Here we have taken $\rho_1 = 0.4$.

$$\begin{aligned}
v &= 246\text{GeV}, v_R \in [10^4, 10^6] \text{ GeV}, \tan \beta = \tan 10^{-3} \\
\lambda_1 &= 0.13, \lambda_2 = 0, \lambda_3 \in [0, 2], \lambda_4 = 0 \\
\rho_1 &\in [0, 0.5], \rho_2 \in [0, 2], \rho_3 \in [1, 2], \rho_4 = 0 \\
\alpha_1 &= 0, \alpha_2 \in [0, 0.5], \alpha_3 \in [0, 1] \\
\beta_1 &= \beta_2 = \beta_3 = 0
\end{aligned} \tag{3.9}$$

We randomly generate 100 sample points within these limits and check for the global minima of the potential in Eq. 2.14 numerically using Mathematica’s **NMinimize** function. Note that the temperature correction term in Eq. 2.15 as a function of r , is not entirely smooth and may contain many local minima of negligible depth; but they might confuse the **NMinimize** function while finding the global minima of the effective potential. Therefore we approximate the effective potential by a smooth polynomial function at different temperatures before minimizing it. We tally these results with *CosmoTransitions* [69] and verify the type

	BP1	BP2	BP3
v/GeV	246	246	246
v_R/GeV	10^4	10^5	10^6
$\tan\beta$	0.001	0.001	0.001
λ_1	0.13	0.13	0.13
λ_2	0	0	0
λ_3	1.95024	0.66708	1.548816
λ_4	0	0	0
ρ_1	0.40055	0.411194	0.350746
ρ_2	0.88258	0.63584	0.847746
ρ_3	1.35815	1.711196	1.14436
ρ_4	0	0	0
α_1	0	0	0
α_2	0.27152	0.340437	0.2123735
α_3	0.82883	0.603991	0.09274
$\beta_{1,2,3}$	0	0	0
g	0.65	0.65	0.65
$g_{\text{B-L}}$	0.4324	0.4324	0.4324
y_t	0.95	0.95	0.95
y_M	1	1	1

Table 1: Benchmark points for SOPT

of phase transitions. Our strategy differs from [51] as in we are not interested in FOPTs, therefore we are not calculating the bounce solutions using CosmoTransitions. Rather we use CosmoTransitions to mainly look for a continuous transition VEV from $r = 0$ at high temperature to $r = v_R(T)$ at low temperature. This would imply a second-order or a *cross-over* phase transition, which we are interested in. Out of the 100 samples, we get 78 successful phase transitions out of which 65 are FOPTs and 9 are SOPTs, and the remaining are a mixture of both. We take 3 of those SOPT points as benchmark points BP1, BP2, BP3 given in Table 1 with energy scales $v_R = 10^4, 10^5, 10^6$ GeV respectively for the GW considerations. But first, we briefly discuss GWs from FOPT in the next section for completeness.

Assuming the DWs vanish within the radiation-dominated era, the peak amplitude and the peak frequency of the GWs produced, as seen at the present time, are given by [70, 71],

$$\Omega_{\text{gw}} h^2 (t_0)_{\text{peak}} \simeq 5.20 \times 10^{-20} \times \tilde{\epsilon}_{\text{gw}} \mathcal{A}^4 \left(\frac{10.75}{g_*} \right)^{1/3} \left(\frac{\sigma_{\text{wall}}}{1\text{TeV}^3} \right)^4 \left(\frac{1\text{MeV}^4}{\delta V} \right)^2 \quad (3.10)$$

$$f_{\text{peak}} \simeq 3.99 \times 10^{-9} \mathcal{A}^{-1/2} \left(\frac{1\text{TeV}^3}{\sigma_{\text{wall}}} \right)^{1/2} \left(\frac{\delta V}{1\text{MeV}^4} \right)^{1/2} \text{ Hz} \quad (3.11)$$

where t_0 denotes the present time. \mathcal{A} is the area parameter $\simeq 0.8$ [71, 72] arising from Z_2 parity breaking of the LRSM, and $\tilde{\epsilon}_{\text{gw}}$ is called the efficiency parameter $\simeq 0.7$ [71]. g_* is

the relativistic degrees of freedom at the time of the DW decay, $g^* = 134$ in our case. The spectrum is approximately given by,

$$\Omega_{\text{GW}} \simeq \Omega_{\text{GW}}|_{\text{peak}} \times \begin{cases} \left(\frac{f_{\text{peak}}}{f}\right) & \text{for } f > f_{\text{peak}} \\ \left(\frac{f}{f_{\text{peak}}}\right)^3 & \text{for } f < f_{\text{peak}} \end{cases} \quad (3.12)$$

We plot the GW spectrum for different benchmark points (as given in Table 1) in Fig. 2. The 3 benchmark points (BP1, BP2, BP3) in Fig. 2 stands for $v_R = 10^4, 10^5, 10^6$ GeV respectively with $\epsilon = 2 \times 10^{-26}$. These signals are detectable at the PTA experiments. Fig. 3, shows the GW spectrum for BP2 with different biases. Note that the parameter ρ_1 is primarily responsible for determining the strength of the phase transition. Especially for bigger values of $\rho_1 \gtrsim 0.3$, the phase transition seems to be second order or weak first order in nature, as can be seen in our benchmark points. Considering this fact, we considered another set of benchmark points with $\rho_1 = 0.4$ and $(\eta, \epsilon) = (10^{10}\text{GeV}, 10^{-17}), (10^{12}\text{GeV}, 10^{-13}), (10^{13}\text{GeV}, 10^{-11})$ which should give detectable GW peaks at the interferometers as seen in Fig. 4.

4 Numerical Simulation

4.1 Equation of Motion

We consider the tree level potential as in Eq. (2.13) to simulate domain wall decay (see [52]). It is symmetric under $r \rightarrow -r$. It has two degenerate minima, at $\pm\eta$. The height of the potential barrier is $\Delta V \approx \rho_1 \eta^4/4$. The evolution of the field in an expanding FLRW metric is given by the Klein-Gordon equation,

$$\ddot{r} + H\dot{r} - \frac{\nabla^2}{a^2}r + \frac{dV}{dr} = 0 \quad (4.1)$$

where dot denotes derivative w.r.t. t and $a = a(t)$ is the scale factor. This equation also describes the evolution of domain walls.

We use the notation of [52] and in the appendix A we summarize the methodology of the calculation, which utilizes the Green's function method. The energy density of GW is given by Eq. (A.14). Replacing the ensemble average by an average over the volume of the comoving box, we obtain,

$$\rho_{\text{gw}} = \frac{1}{32\pi G a^4} \frac{1}{V} \int \frac{d^3\mathbf{k}}{(2\pi)^3} \bar{h}'_{ij}(\tau, \mathbf{k}) \bar{h}'_{ij*}(\tau, \mathbf{k}) \quad (4.2)$$

Substituting the form of \bar{h}_{ij} from Eq. (A.12) and (A.13), upto first order of aH , we obtain,

$$\rho_{\text{gw}} = \frac{2\pi^2 G}{a^4 V} \int \frac{d^3\mathbf{k}}{(2\pi)^3} \frac{1}{k^2} \times \sum_{ij} \left\{ \left| \int_{x_i}^{x_f} dx' \sqrt{x'} a(x') N_\nu(x') T_{ij}^{\text{TT}}(\tau', \mathbf{k}) \right|^2 + \left| \int_{x_i}^{x_f} dx' \sqrt{x'} a(x') J_\nu(x') T_{ij}^{\text{TT}}(\tau', \mathbf{k}) \right|^2 \right\} \quad (4.3)$$

where we have used approximations for $k\tau \gg 1$,

$$J_\nu(k\tau) \rightarrow \sqrt{\frac{2}{\pi(k\tau)}} \cos\left(k\tau - \frac{\nu\pi}{2} - \frac{\pi}{4}\right), \quad N_\nu(k\tau) \rightarrow \sqrt{\frac{2}{\pi(k\tau)}} \sin\left(k\tau - \frac{\nu\pi}{2} - \frac{\pi}{4}\right) \quad (4.4)$$

and averaged over a period of oscillation of $\bar{h}_{ij}(\tau, \mathbf{k})$ with time. The fraction of energy density of GWs given by Eq. (A.15) becomes,

$$\Omega_{\text{gw}}(k, t) = \frac{2G^2k}{3Va(t)^4H(t)^2} \int d\Omega_k \times \sum_{ij} \left\{ \left| \int_{x_i}^{x_f} dx' \sqrt{x'} a(x') N_\nu(x') T_{ij}^{\text{TT}}(\tau', \mathbf{k}) \right|^2 + \left| \int_{x_i}^{x_f} dx' \sqrt{x'} a(x') J_\nu(x') T_{ij}^{\text{TT}}(\tau', \mathbf{k}) \right|^2 \right\} \quad (4.5)$$

where Ω_k is a unit vector representing the direction of \mathbf{k} and $d\Omega_k = d\cos\theta dr$. The TT part of the stress-energy tensor is computed by applying the projection operator in the momentum space,

$$\begin{aligned} T_{ij}^{\text{TT}}(\tau, \mathbf{k}) &= \Lambda_{ij,kl}(\hat{k}) T_{ij}(\tau, \mathbf{k}) \\ &= \Lambda_{ij,kl}(\hat{k}) \{ \partial_k r \partial_l r \}(\tau, \mathbf{k}) \end{aligned} \quad (4.6)$$

$$\Lambda_{ij,kl}(\hat{k}) = P_{ik}(\hat{k}) P_{jl}(\hat{k}) - \frac{1}{2} P_{ij}(\hat{k}) P_{kl}(\hat{k}) \quad (4.7)$$

$$P_{ij}(\hat{k}) = \delta_{ij} - \hat{k}_i \hat{k}_j \quad (4.8)$$

where $\hat{k} = \mathbf{k}/|\mathbf{k}|$, and $\{ \partial_k r \partial_l r \}(\tau, \mathbf{k})$ is the Fourier transform of $\partial_k r(\tau, \mathbf{x}) \partial_l r(\tau, \mathbf{x})$.

4.2 Simulation Setup

The simulation takes place in a cuboid of size $L_x = L_y = L_z = b$ in terms of η^{-1} , discretized into $N^3 = 256^3$ lattice points. Our simulation box is a comoving box, which also expands with the expansion of the universe. The problem with this setup is that, the dynamical range of the simulation is limited. This is due to the fact that we want our comoving box to be bigger than the correlation length, and also want to resolve the domain wall width, at all times during the simulation. Domain wall width remains constant in real space, i.e. decreases as $a(t)^{-1}$ within the simulation box.

Let our physical lattice spacing be $\delta x_{phy} = a(t) \times b/N = a(t) \times 50/256$. Assuming initial time of simulation $t_i = 1$ and setting $a(t_i) = 1$, the ratio of domain wall width to lattice spacing is,

$$\frac{\delta_w}{\delta x_{phy}} = \frac{N}{b\rho_1^{1/2}} \left(\frac{t}{t_i} \right)^{-\gamma} \quad (4.9)$$

where γ is from Eq. (A.6). In our case, the entire process occurs in the radiation dominated universe ($\gamma = 1/2$), and we choose $\rho_1 = 0.4$, $b = 50$ and vary ϵ from 0 to 0.015 for the simulations. Corresponding to each ϵ , we get an approximate wall decay time t_{dec} from Eq. (3.5). But we see that for $t > 61$ (in units of η^{-1}) the above ratio is > 1 , which means that

the walls are not resolvable anymore. This limits the upper bound on the time integral of the GW calculation in Eq. (4.5) to be the resolution time $t = t_{\text{res}} = 61$, i.e. we consider the source to be active from $t = 1$ to $t = 61$. Beyond that we will get unphysical results. We chose the maximum time of simulation to be 151 to see how the spectrum changes beyond $t = 61$ and plot them in figures 7 and 8. The different plots in each graph corresponds to what upper limit we take in GW calculation in Eq. (4.5). Ideally t_{dec} should be smaller than 61 in our simulation to obtain realistic results but we also consider larger t_{dec} and interpret the results carefully as discussed in Sec. 4.4.

The correlation length determines the initial size of the domains. Assuming m_r and T_c to be of the order of η , dimensionally we can find $\xi_{\text{causal}}/\eta^{-1} \sim \left(\frac{M_{\text{pl}}}{\eta}\right)^{1/3}$, which is around 10 for $\eta = 10^{16}$ GeV and 1000 for $\eta = 10^{10}$ GeV. So we take $\eta = 10^{16}$ GeV for our simulation so that the domain sizes are of the order $\mathcal{O}(10)$.

Spectrum calculation procedure:

1. Simulate the field for a specific time steps to obtain $r(\tau, \mathbf{x})$.
2. Calculate $\{\partial_k r \partial_l r\}(\tau, \mathbf{k})$ by taking **Discrete Fourier Transform (DFT)** of $\partial_k r(\tau, \mathbf{x}) \partial_l r(\tau, \mathbf{x})$
3. Calculate $T_{ij}^{\text{TT}}(\tau, \mathbf{k})$ using Eq. (4.6)-(4.8).
4. Perform the time integration in Eq. (4.5) and the sum over i, j . We used a simple Simpson's 3/8th rule for the time integration.
5. Perform the angular integration $\int d\Omega_k$ using **Monte Carlo method**. Multiply by appropriate constant as in Eq. (4.5).

4.2.1 Initial Field Configuration

We assume that domain walls are already produced at t_i with characteristic length scale given by the correlation length, motivated by Eq. (2.22). So we take a Sin function with the wavelength corresponding to twice the correlation length at the initial time as our dominant mode, i.e. $k_{\text{dominant}} = \pi/\xi_{\text{causal}}$. One wavelength of the Sin function consists of two domains of opposite vacua. We randomize the configuration by adding 4-5 more modes to it with small coefficients. Finally we take a Tanh of this series of Sin functions which squeezes the rise and fall of the Sin curves, as a good model of the domain wall kink. The final results are obtained as broad dependence of the power on frequency and are insensitive to minor changes in the initial conditions. The needed configuration corresponds to a mesh of cubical domains where each domain is surrounded by the opposite kind of domains, and can be created by defining the initial field values as,

$$r(x, y, z) = \tanh \left[N_{\text{norm}} \sum_{n=1}^{i=5} C_n \sin(k_n x + \phi_i) \sin(k_n y + \psi_i) \sin(k_n z + \chi_i) / \delta_{\text{wall}} \right] \quad (4.10)$$

where N_{norm} is a normalizing factor, $C_1 = 1$ and the rest of the C_i are small numbers of the order $\mathcal{O}(10^{-1})$. $k_n = \pi n / \xi_{\text{causal}}$ represents the initial characteristic comoving wavenumber.

Every dimensional parameter is scaled by η . Finally ϕ_i, ψ_i, χ_i are random phases. It turns out that the resulting spectrum is independent of the exact initial configuration rather on the dominant fluctuation scales.

In figure 5, the evolution of the domain wall network is shown for $\epsilon = 0$ and $\epsilon = 0.007$. The effect of the bias is clearly seen as false domains reduce in size and domain walls decay, while there's no preferred domain in the zero bias case.

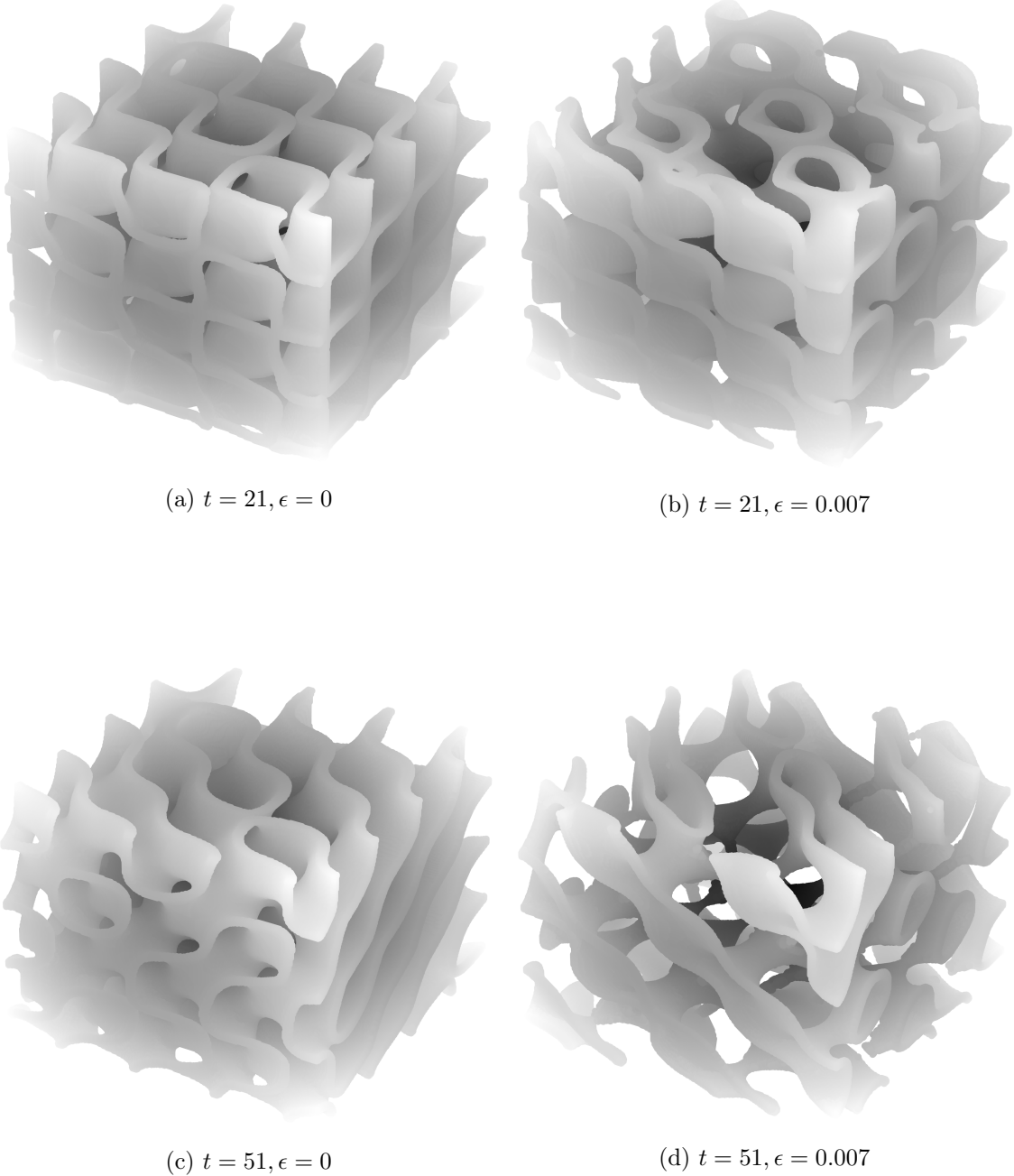


Figure 5

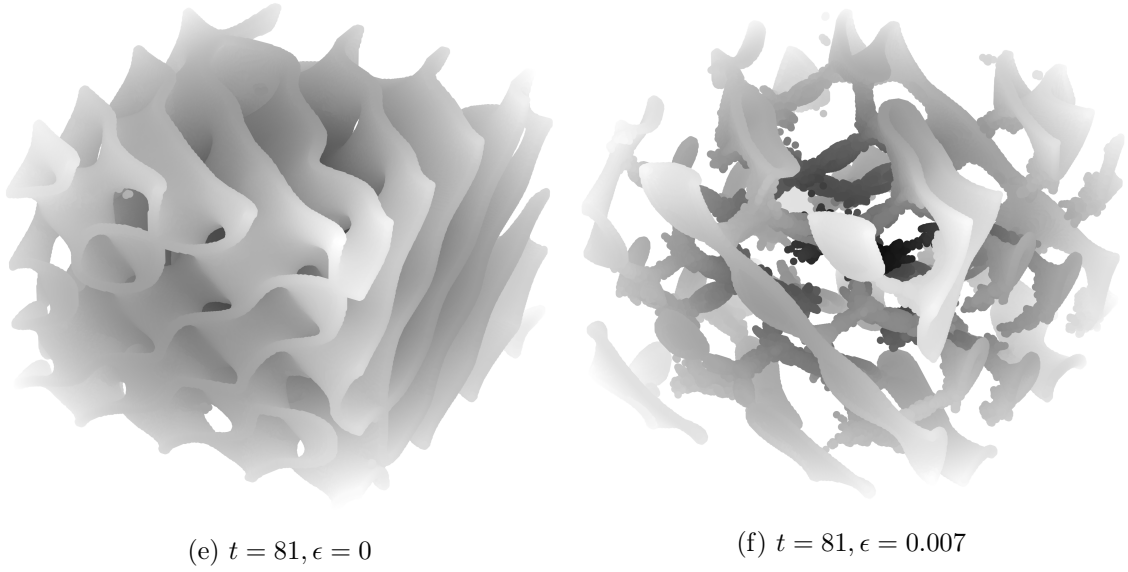


Figure 5

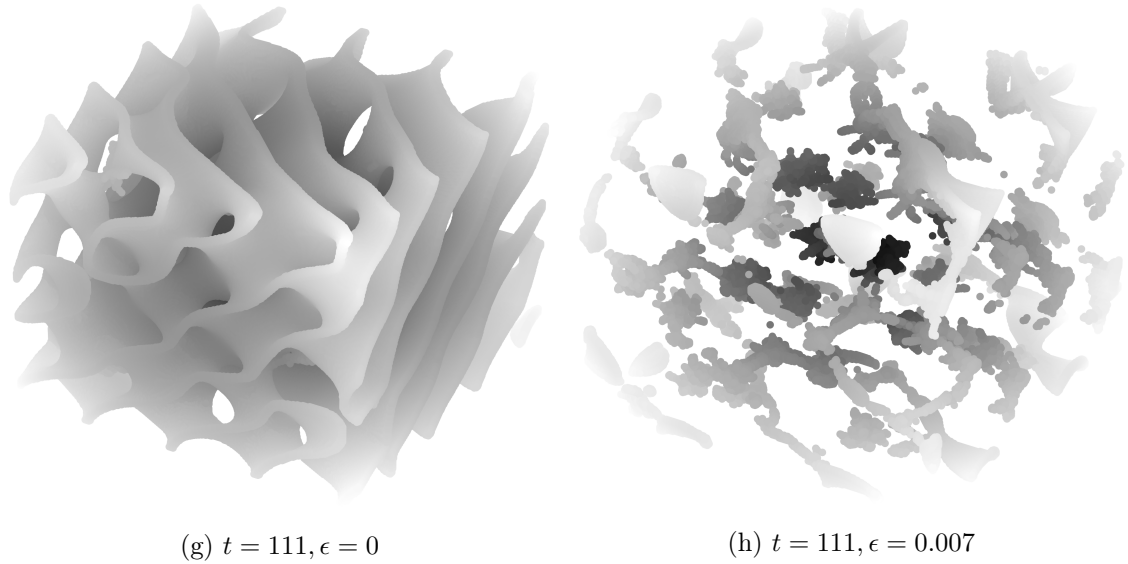


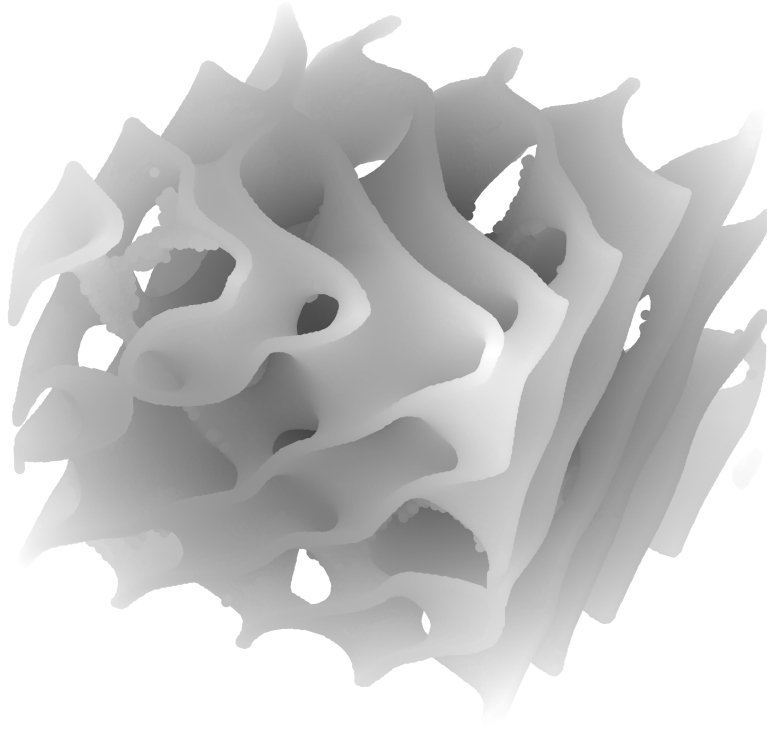
Figure 5

4.3 Scaling Regime

An important feature of domain wall evolution without bias is the era or scaling solutions, when the characteristic length scales like radius of curvature of domain walls or domain size is given by Hubble radius,

$$R \sim H^{-1} \sim t \quad (4.11)$$

This phase of evolution is found both numerically [73–78] and analytically [79–81] in the literature, and it corresponds to “at least one domain wall per horizon” scenario. While in



(i) $t = 141, \epsilon = 0$

Figure 5: Evolution of domain walls for $\epsilon = 0$ on the left column and $\epsilon = 0.007$ on the right column. Image (i) is the final form of the no-bias case after the simulation.

the scaling regime, the energy density of the domain walls is given by,

$$\rho_{\text{wall}} \sim \sigma_{\text{wall}} R^2 / R^3 \sim \sigma_{\text{wall}} / t \quad (4.12)$$

with σ_{wall} given in Eq. (3.3), Eq. (4.12) can be expressed as,

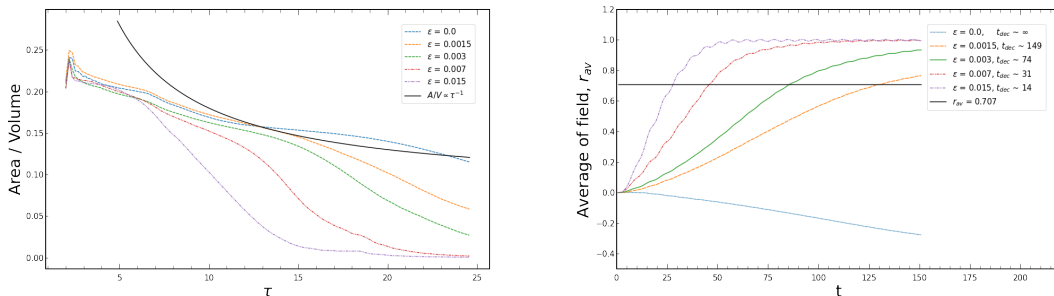
$$A/V \propto \tau^{-1} \quad (4.13)$$

where A/V is the comoving area density of the walls and τ is the conformal time. To calculate this quantity we define a wall to be the surface where field value is 0. Therefore, to measure the surface area of walls in the 3D lattice, first we have to figure out where the field crosses zero value within the lattice. To do this, let us call two lattice points that are nearest neighbours as *links*. These links are oriented in x, y, z directions and we measure the signs of the field at the two ends of each link. If the signs are different at the two ends, we have found a zero crossing of the field. For all such possible links at all the lattice points within the cube, we do the same and assign a variable δ_{\pm} to each link, which takes on value +1 if we found a zero crossing, otherwise 0. Once we find such a link which penetrates a wall, we add one unit grid area (area of the square made by nearest points) to the total surface area of walls, but divided by a weight factor. The weight factor must be the average of number density of points on the surface, based on the orientation of the surface at the location of

the link. The orientation can be found through the unit normal vector to the wall (given by the gradient of the field) at that location. Finally, we sum all such contributions from all the links with $\delta_{\pm} = 1$ to obtain the total wall area [73],

$$A = \Delta A \sum_{\text{all links}} \delta_{\pm} \frac{|\nabla\phi|}{|\partial_x\phi| + |\partial_y\phi| + |\partial_z\phi|} \quad (4.14)$$

where ΔA is the unit grid area. In our case $\Delta A = \Delta x^2 = \Delta y^2 = \Delta z^2 = (b/N)^2$. We calculate this quantity divided by volume b^3 of the cube at different times and plot in Fig. 6. The walls seems to enter the scaling regime after $\tau \sim 10$.



(a) Area density with conformal time.

(b) Mean field value with time.

Figure 6: Evolution of a) comoving area density with conformal time and b) mean field value with t . In a), for no-bias case the walls seems to follow scaling solutions after $\tau \sim 10$ where area density varies as τ^{-1} as mentioned in Sec. 4.3. In b) we verify the equation for decay time (3.5) upto $\mathcal{O}(1)$ by measuring the mean field value with time for different simulations. The mean crosses the $r = 1/\sqrt{2}$ line at around $t = t_{\text{dec}}$.

4.4 Gravitational Wave Spectrum

We normalize the amplitude of GW given in Eq. (4.5) by,

$$\Omega_{\eta} \equiv \frac{\rho_{gw}^{\eta}}{\rho(t_i)} = \frac{8\pi}{3\beta^2} G^2 \eta^4 \quad (4.15)$$

where $\rho_{gw}^{\eta} = G\eta^6$ is the energy density of a source of characteristic scale η estimated from Quadrupole approximation, and $\rho(t_i) = 3H^2(t_i)/8\pi G = 3\beta^2\eta^2/8\pi G$ is the critical energy density at the initial time. We plot the energy spectrum for the no bias case in Fig. 7 and with different biases in Fig. 8. The horizontal axis is the amplitude of the comoving wave-vector. It is related to the frequency as in Eq. (A.16). Notice that in the Monte Carlo method used to perform the angular integration $d\Omega_k$, we define the shell of radius k and average out the values of the fields at the lattice points within that shell. Therefore in the small k region, number of points within the shell is also small which generates statistical error in the calculation, i.e. the lower k range of $\mathcal{O}(0.1)$, where the peak occurs, is not properly resolvable. We plot the error bars for the Monte Carlo integration to show the

statistical uncertainties in the calculation. Other sources of error include numerical errors from the usage of a simple difference method for simulation and Simpson’s rule for the time integration. Therefore it is difficult to provide conclusive remarks about the spectrum with our small dynamical range. However, we can deduce some information about the spectrum as follows:

1. As discussed in Sec. 4.2 we fit the curve (solid black line) at $t \sim t_{\text{res}} \sim 61$ for different cases. We understood that beyond t_{res} , we will get unphysical results. Those unphysical results manifest in the graphs as overall higher amplitude if $t_{\text{dec}} > t_{\text{res}}$, and resonance, seen as a bump around $k \sim \mathcal{O}(10)$, corresponding to the wall width. The reason for the resonance is that the wall width becomes equivalent or greater than the physical lattice spacing beyond t_{res} . Therefore we will consider the fitted line to be the actual spectrum from the simulation.
2. It is seen that the spectrum peaks at around $k \sim 0.4 - 0.5$ which corresponds to the Hubble size at the time of GW production, $k_h/a(t) = 2\pi H(t)$ at $t \sim 61$, as seen from the fitted line.
3. The spectrum shows a dependence of k^{-1} beyond the peak as seen in Fig. 7 for the no-bias case. If we evolve the field with a bias explicitly, an enhancement towards the high frequency region is seen which can be interpreted as contribution coming from smaller sized walls as the simulation proceeds. In the no-bias case, walls don’t crumble to give such contribution. For observation in experiments, such high frequency enhancement is irrelevant since we are interested only in the peak at k_h . Thus we conclude that the spectrum varies as k^{-1} for $k > k_h$.
4. Now due to the high error in the small k range, the behavior of the spectrum in that region is unclear. Therefore we assume a k^3 dependence for $k < k_h$ considering requirements for causality [82]. These conclusions match with [70, 71], therefore in Sec. 3, we use the same general formulas as given in them for the GW spectrum generated at arbitrary scale with arbitrary bias, as seen today. The formulas are given in (3.10) and (3.11).

5 Gravitational waves from First-order Phase Transition

We begin with the contributions from a standard FOPT for our model, since the additional contribution due to the residual DW of the Degenerate Field FOPT arise independently. Gravitational waves spectrum from FOPT is characterised by two parameters α and β , corresponding to the strength of the phase transition and the inverse rate of tunnelling. In this section, we will give relevant definitions of these two parameters and speculate the observability of the GW spectrum for typical values for them.

First order phase transition (FOPT) takes place through *nucleation* of bubbles within which r takes the true VEV, $v_R(T)$. The field r tunnels from a metastable state $v_R(T) = 0$ to the stable ground state $v_R(T) \neq 0$ considering enough *supercooling*. These bubbles are

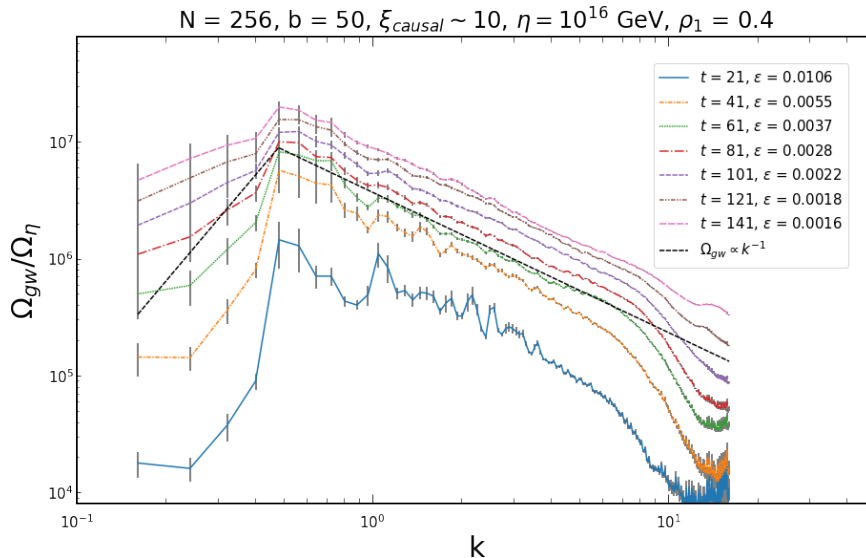


Figure 7: Normalized GW spectrum vs comoving wavenumber with no bias. Assuming the walls suddenly vanish at different t , we can calculate the bias for the corresponding graph from Eq. (3.5) as shown in the legend. Error is calculated as σ/\sqrt{N} and shown by error bars. The spectrum peaks around $k \sim k_h \sim \mathcal{O}(0.4 - 0.5)$, corresponding to the Hubble radius for $t \sim 61$. The black dashed line is a curve fit at $t = t_{res} = 61$ which shows a dependence of k^{-1} at the high frequency region. Note that high errors in the low frequency region makes it difficult to exactly see the dependence of the spectrum for small k . Therefore from causality requirements [82] we assume a k^3 dependence at $k < k_h$. Beyond t_{res} , we get unphysical results as discussed in Sec. 4.2.

$O(4)$ symmetric *bounce solutions* [83]. After nucleation, these bubbles of true VEV expands through the plasma in the expanding metastable Universe, and the bubble walls attain a terminal velocity close to the speed of light. The nucleation rate of bubbles is given by [44, 45, 51, 84],

$$\Gamma(T) \simeq T^4 \left(\frac{S_3}{2\pi T} \right)^{\frac{3}{2}} e^{-S_3/T} \quad (5.1)$$

where S_3 is the three-dimensional Euclidean action evaluated for the bounce solution which is obtained by solving the equation of motion,

$$\frac{d^2 r}{dx^2} + \frac{2}{x} \frac{dr}{dx} = \frac{dV_{\text{eff}}(r, T)}{dr} \quad (5.2)$$

with boundary conditions $dr/dx = 0$ at $x = 0$ and $r \rightarrow 0$ as $x \rightarrow \infty$ where x denotes the 3D radial coordinate. Next, the *nucleation temperature* T_n , is the temperature at which there's at least one bubble created per horizon volume,

$$\int_{T_n}^{T_c} \frac{dT}{T} \frac{\Gamma(T)}{H(T)^4} = 1 \quad (5.3)$$

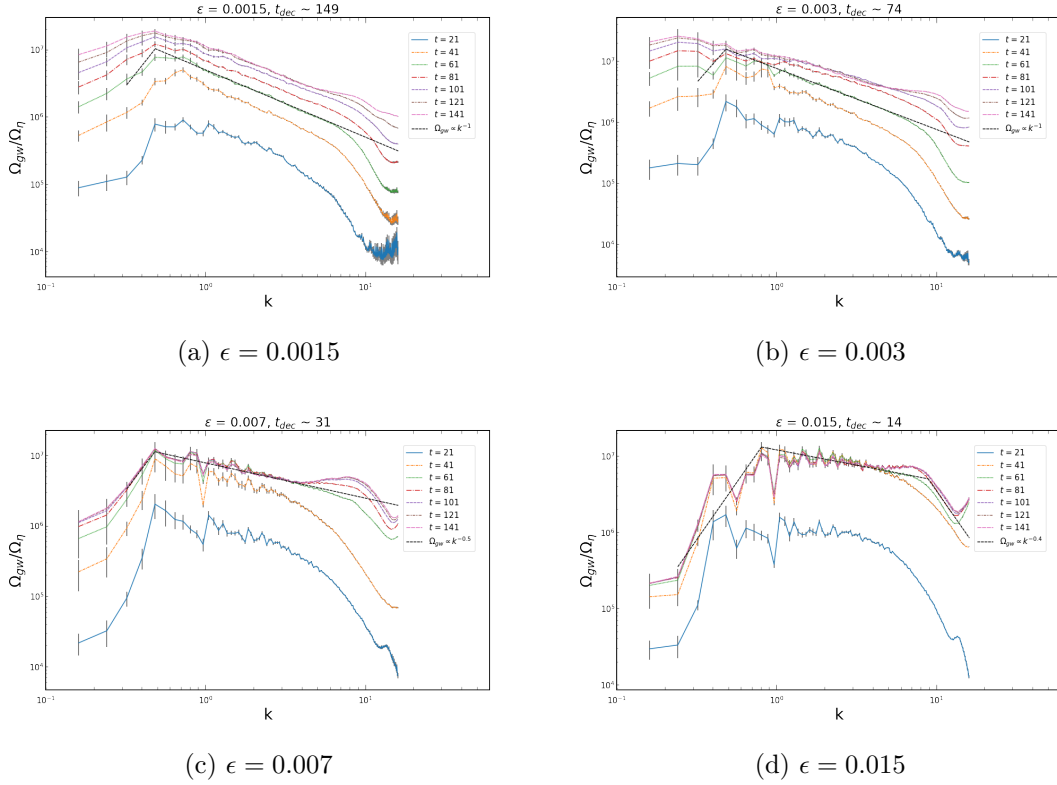


Figure 8: Spectrum for different biases. The wall decay time t_{dec} for each case is calculated using the formula (3.5). The curve fit line has smaller slope compared to that in Fig. 7, which shows an enhanced contribution in the high frequency region as compared to the no-bias case. More the bias more the enhancement and at $\epsilon = 0.015$, the spectrum is almost flat between the Hubble frequency and wall width frequency around $k \sim \mathcal{O}(10)$. This enhancement comes from the small sized walls towards the end of the simulation.

where the Hubble parameter is given by,

$$H(T)^2 = \frac{\rho_{\text{rad}}(T) + \rho_{\text{vac}}(T)}{3\mathcal{M}_{\text{Pl}}^2} = \frac{1}{3\mathcal{M}_{\text{Pl}}^2} \left(\frac{\pi^2}{30} g_* T^4 + \Delta V(T) \right) \quad (5.4)$$

with $g_* = 134$ is the relativistic degrees of freedom for our model and $\mathcal{M}_{\text{pl}} = 2.435 \times 10^{18}$ GeV is the reduced Planck Mass. Vacuum energy density $\rho_{\text{vac}}(T)$ is calculated as $\Delta V(T) := V_{\text{eff}}(0, T) - V_{\text{eff}}(v_R(T), T)$. Once we have T_n , we can define the parameters [49, 85],

$$\alpha = \frac{1}{\rho_{\text{rad}}(T_n)} \left(\Delta V(T_n) - \frac{T_n}{4} \frac{\partial \Delta V(T)}{\partial T} \Big|_{T=T_n} \right) \quad (5.5)$$

which characterizes the strength of the FOPT; and the inverse duration of the transition given by,

$$\beta = H(T_n) T_n \cdot \frac{d(S_3/T)}{dT} \Big|_{T=T_n} \quad (5.6)$$

For strong FOPT, the typical values for these two parameters for our model are, $\alpha \in [0.001, 0.1]$ and $\beta/H_* \in [10^2, 10^4]$ [86] where $H_* = H(T_n)$. Therefore, in table 2, we take 3 benchmark points randomly within these ranges of α and β , which we will use to plot the GW spectrum.

Now, there are three sources of GWs in case of a first-order phase transition; i) bubble wall collision [87], ii) sound waves [82] and iii) magnetohydrodynamic (MHD) turbulence [88]. Even though nucleated bubbles are $O(4)$ symmetric, the spherical symmetry is broken when the bubbles collide, which is the basic requirement for GW production. Thus, the total GW spectrum is given by,

$$h^2\Omega_{\text{GW}} \simeq h^2\Omega_r + h^2\Omega_{\text{sw}} + h^2\Omega_{\text{turb}} \quad (5.7)$$

The first term is the contribution from bubble collision which can be calculated from the field evolution. The second and third terms are the sound wave and MHD turbulence contributions respectively.

5.1 Bubble Collision

Assuming the *envelope approximation* [89], the contribution from bubble collision is given by [3, 90, 91],

$$h^2\Omega_{\text{env}}(f) = 1.67 \times 10^{-5} \left(\frac{H_*}{\beta}\right)^2 \left(\frac{\kappa_c \alpha}{1+\alpha}\right)^2 \left(\frac{100}{g_*}\right)^{\frac{1}{3}} \left(\frac{0.11v_w^3}{0.42+v_w^2}\right) \frac{3.8(f/f_{\text{env}})^{2.8}}{1+2.8(f/f_{\text{env}})^{3.8}} \quad (5.8)$$

where $H_* = H(T_n)$ and the efficiency factor κ_c is given by [48],

$$\kappa_c = \frac{0.715\alpha + \frac{4}{27}\sqrt{\frac{3\alpha}{2}}}{1+0.715\alpha} \quad (5.9)$$

In the above equation v_w is the wall velocity which we assume to be unity for calculations. The peak frequency is given by

$$f_{\text{env}} = 16.5 \times 10^{-6} \left(\frac{0.62}{1.8-0.1v_w+v_w^2}\right) \left(\frac{\beta}{H_*}\right) \left(\frac{T_n}{100\text{GeV}}\right) \left(\frac{g_*}{100}\right)^{\frac{1}{6}} \text{ Hz} \quad (5.10)$$

5.2 Sound Waves

The movement of the DWs through the plasma creates pressure waves in the plasma. The contribution of such sound waves to GW is given from numerical fit [3, 92],

$$h^2\Omega_{\text{sw}}(f) = 2.65 \times 10^{-6} \left(\frac{H_*}{\beta}\right) \left(\frac{\kappa_{\text{sw}}\alpha}{1+\alpha}\right)^2 \left(\frac{100}{g_*}\right)^{\frac{1}{3}} v_w \left(\frac{f}{f_{\text{sw}}}\right)^3 \left(\frac{7}{4+3(f/f_{\text{sw}})^2}\right)^{7/2} \quad (5.11)$$

where the efficiency factor κ_{sw} is given by [93],

$$\kappa_{\text{sw}} = \alpha(0.73 + 0.083\sqrt{\alpha} + \alpha)^{-1} \quad (5.12)$$

The peak frequency is given by,

$$f_{\text{sw}} = \frac{1.9 \times 10^{-5}}{v_w} \left(\frac{\beta}{H_*}\right) \left(\frac{T_*}{100\text{GeV}}\right) \left(\frac{g_*}{100}\right)^{\frac{1}{6}} \text{ Hz} \quad (5.13)$$

	BPF1	BPF2	BPF3
T_n/GeV	10^4	10^5	10^6
α	0.0042	0.064	0.12
β/H_*	4087	156	898

Table 2: Benchmark points for FOPT

5.3 MHD Turbulence

Turbulent motion of the fully ionized plasma also contributes to the GW spectrum, modelled by [3, 94, 95],

$$h^2\Omega_{\text{turb}}(f) = 3.35 \times 10^{-4} \left(\frac{H_*}{\beta}\right) \left(\frac{\kappa_{\text{turb}} \alpha}{1 + \alpha}\right)^{\frac{3}{2}} \left(\frac{100}{g_*}\right)^{1/3} v_w \frac{(f/f_{\text{turb}})^3}{[1 + (f/f_{\text{turb}})]^{\frac{11}{3}} (1 + 8\pi f/h_*)} \quad (5.14)$$

where $\kappa_{\text{turb}} = 0.05\kappa_{\text{turb}}$ [93] and,

$$h_* = 16.5 \cdot 10^{-6} \left(\frac{T_n}{100\text{GeV}}\right) \left(\frac{g_*}{100}\right)^{1/6} \text{ Hz} \quad (5.15)$$

The peak frequency is given by,

$$f_{\text{turb}} = \frac{2.7 \times 10^{-5}}{v_w} \left(\frac{\beta}{H_*}\right) \left(\frac{T_*}{100\text{GeV}}\right) \left(\frac{g_*}{100}\right)^{\frac{1}{6}} \text{ Hz} \quad (5.16)$$

5.4 Degenerate field FOPT

We now summarise the results from all the above listed contributions, Fig. 9 shows the GW spectrum from FOPT for the 3 benchmark points BPF1, BPF2, BPF3 with different nucleation temperature T_n , as given in Table 2. We see that the peak of BPF2 is detectable in BBO and DECIGO whereas BPF1 and BPF3 have no chance of getting detected in one of these experiments. In Fig. 10, we show GW peaks for typical values of α and β/H_* obtained from our model with different T_n , and color code them according to their observability in the future. The red dots correspond to detectable peaks whereas the blue dots represent unobservable peaks in BBO, DECIGO, CE, ET, and LISA.

The FOPT bubble contributions need to be supplemented by the contribution from the disintegration of the residual DW. For the benchmark points considered here, it is possible to add this contribution from the CHL-SOPT calculation of Fig. 2 since at least the mass scales considered there are the same as used for the benchmark points here. In Fig. 11 we plot doubly peaked spectra from typical strong FOPTs at different scales, for the benchmark points (BPDs) 1, 2, 3 given in Table 3. The two peaks correspond to the FOPT peak and the decay of residual domain walls. In Fig. 12 we plot the same for a high scale BPD, $\eta \sim 10^{10}\text{GeV}$. It is seen from Fig. 11 that a direct verification of degenerate 2-field FOPT is marginally possible for low scale L-R models, whereas a high scale case such as in Fig. 12 is beyond the reach of currently planned experiments.

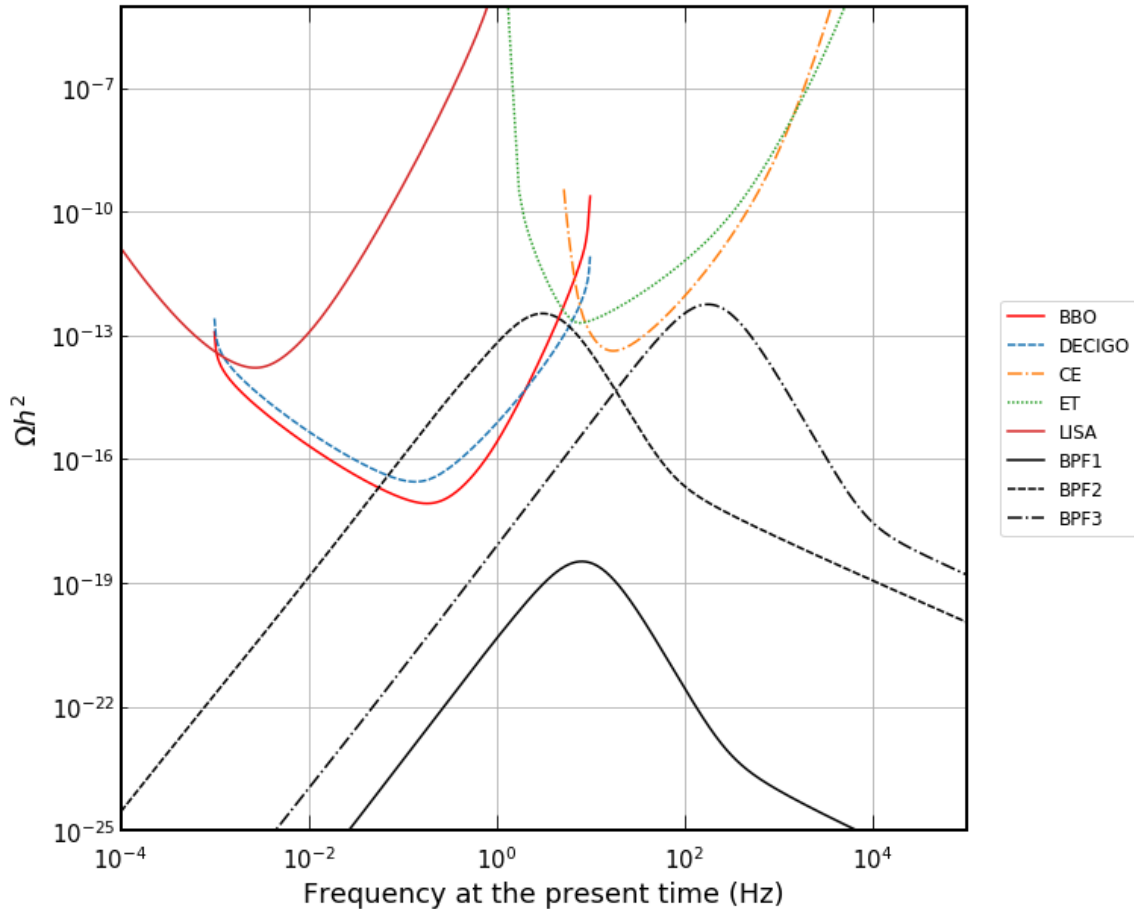


Figure 9: GW spectrum as seen today, from FOPT for BPF1, BPF2, BPF3 with $v_R = 10^4, 10^5, 10^6$ GeV respectively, in comparison to *power-law-integrated-sensitivities* [96] of different experiments.

	BPD1	BPD2	BPD3	BPD4
T_n/GeV	10^4	10^5	10^6	10^{10}
ρ_1	0.1	0.1	0.1	0.1
$\mu_3^2 \sim T_n^2 \rho_1$	10^7	10^9	10^{11}	10^{19}
ϵ	10^{-26}	10^{-26}	10^{-26}	10^{-17}
α	0.1	0.1	0.1	0.1
β/H_*	1000	1000	1000	1000

Table 3: Benchmark points for typical strong FOPT. Here we assumed $T_n \sim \eta$ hence from Eq. (2.11), $\mu_3^2 \sim T_n^2 \rho_1$. The resulting doubly peaked spectra are shown in Figs 11 and 12.

6 Dissociating Parity breaking from LR Symmetry Breaking

In the minimal model we discussed so far, parity \mathcal{P} and LR symmetry are broken simultaneously where the right-handed triplet Δ_R takes a high VEV whereas Δ_L VEV is assumed to

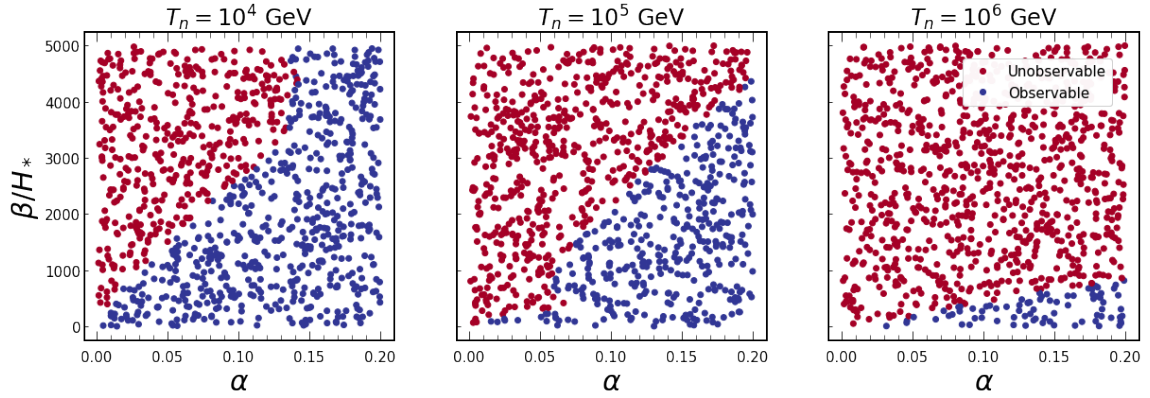


Figure 10: Strength of GW peak for different values of α and β/H_* for $T_n = 10^4, 10^5, 10^6$ GeV. Red dots signify unobservable peaks in BBO, DECIGO, CE, ET and LISA whereas blue dots implies observable signal.

be negligible. This assumption is based on the fact that Standard Model is predominantly left-handed in nature, and what breaks this parity is still unknown. To address this issue, Chang et al [7, 8] described a way to dissociate parity from LR symmetry by adding a scalar χ into the particle content, with negative parity, i.e. $\chi \rightarrow -\chi$ under D -parity transformation. This χ adds extra terms to our tree level potential,

$$V_\chi = -\mu_\chi^2 \chi^2 + \gamma_1 \chi^4 \quad (6.1)$$

$$V_{\chi\Delta} = M_\chi \text{Tr} \left(\Delta_L^\dagger \Delta_L - \Delta_R^\dagger \Delta_R \right) + \gamma_2 \chi^2 \text{Tr} \left(\Delta_L^\dagger \Delta_L + \Delta_R^\dagger \Delta_R \right) \quad (6.2)$$

$$V_{\chi r} = \gamma_2 \chi^2 \text{Tr} \left(r^\dagger r \right) + \gamma_2^1 \chi^2 \left(\text{Det} r + \text{Det} r^\dagger \right) \quad (6.3)$$

In this scenario χ takes a VEV, breaking parity at M_{parity} scale before $SU(2)_R$ is broken at scale M_R . Depending on which minima the field χ takes out of $\pm M_{\text{parity}} = \mu_\chi / \sqrt{2\gamma_1}$ in a region, the Universe becomes left or right-handed in that region, subject to minimal fine-tuning. Since our Universe is left-handed, we want the right-handed regions/domains to vanish eventually. This can be achieved again by making the domain walls unstable by adding a small bias term into the χ potential. If $M_{\text{parity}} \gg M_R$, the contribution from $SU(2)_R$ or $SU(2)_L$ breaking within left-like and right-like domains to the GW background will be negligible compared to the contribution from the χ domain walls. Thus we can assume that this type of dissociated high-energy parity breaking schemes can also be responsible for detectable GW signals.

7 Conclusion

All our calculations have been carried out with a effective potential field with a single field. While we have paid attention to the qualitatively distinct nature of the phase transitions, realistic results need to be supplemented by additional factors. Although we have discussed

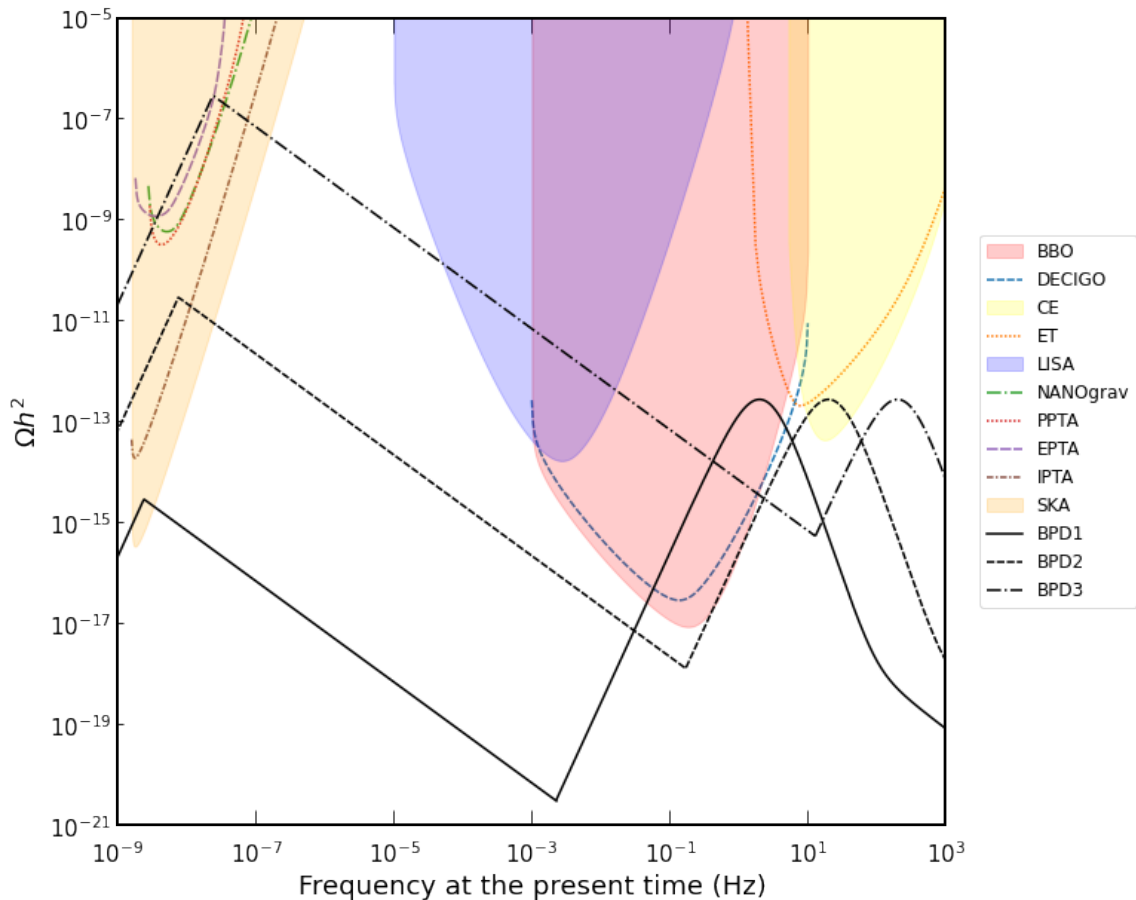


Figure 11: Doubly peaked spectra from strong FOPT for benchmark points 1, 2, 3 given in Table 3. The peak resulting from wall collision, sound waves and MHD turbulence lies generally within the sensitivity of BBO and DECIGO whereas the peak from residual domain wall decay generically occurs at low frequencies accessible to PTA experiments.

the LRSM with two Δ fields our calculations focus on a single field for simplicity of calculations. A supersymmetric version of the LRSM contains a further doubling of these fields, in addition to a few others that might be needed. Thus the power radiated as GW gets a factor of at least 2 if not more for a any realistic model. However since the comparisons with experiments are at present at logarithmic scales, we have fairly representative results.

For the single field case a final summary is provided by Fig. 13. It contains the contour of peak frequency and peak amplitude in the parameter space of η and ϵ . This shows the region of the parameter space where observable signal is produced.

In summary, we have emphasised the qualitatively different considerations which arise with respect to phase transitions when dealing with a theory with left-right symmetry, and similar considerations will apply to the case of $SO(10)$ when the pseudo-defect domain walls are taken into account. In particular, the SOPT case usually not expected to leave behind any signature indeed creates a GW signature. If the parameter space signals an FOPT then in fact we get two separate peaks, one from the usual bubble wall collisions and an

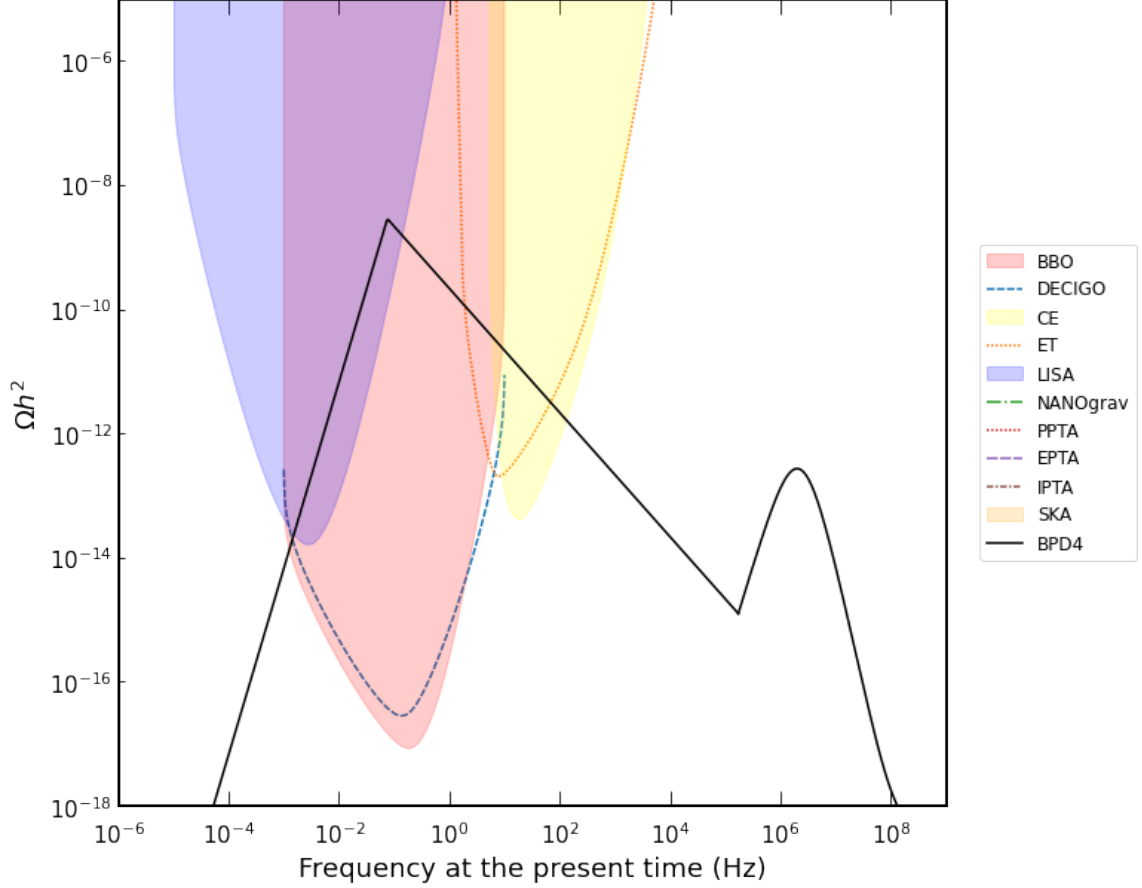


Figure 12: Similar to Fig. 11, for benchmark point 4 of Table 3.

additional peak at much lower frequencies arising from the residual DW that arise due to the presence of two or more degenerate fields present in the theory.

A Appendix

A.1 Rescaling the Field Equation

There's only one energy scale in our theory, η . We can define all other dimensional parameters in terms of η to make our equation dimensionless, eg: $t \rightarrow t\eta$, $x \rightarrow x\eta$, $r \rightarrow r\eta^{-1}$ etc. We assume the evolution takes place entirely in the radiation dominated era such that the scale factor and the Hubble parameter have time dependence

$$a(t) = a_0 t^{1/2} \quad (\text{A.1})$$

$$H(t) = \dot{a}/a = \frac{1}{2t} \quad (\text{A.2})$$

Thus, we make them dimensionless by $a \rightarrow a\eta^{1/2}$, $H \rightarrow H\eta^{-1}$. The rescaled equation is obtained after dividing Eq. (4.1) by η^3 ,

$$\ddot{r} + 3H(t)\dot{r} - \frac{\nabla^2}{a(t)^2}r + \rho_1 r (r^2 - 1) + \epsilon (r^2 - 1) = 0 \quad (\text{A.3})$$

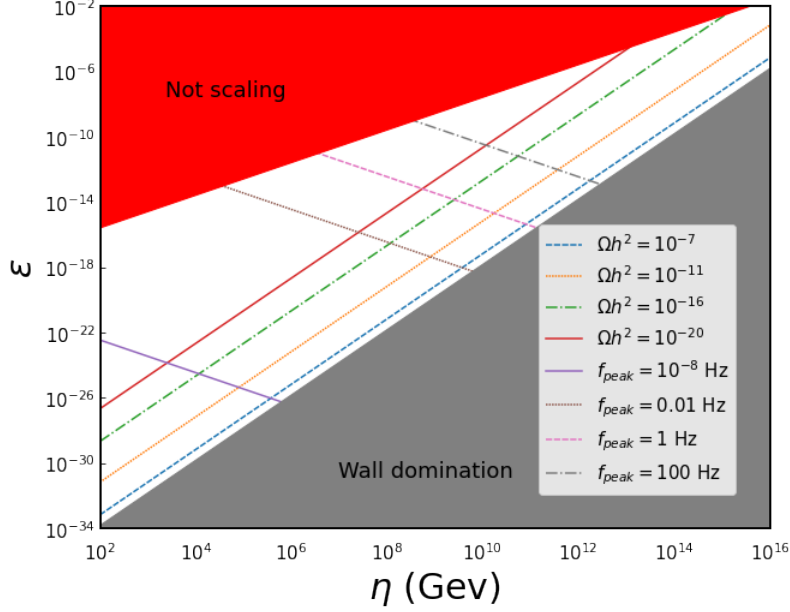


Figure 13: Contour of peak frequency and amplitude in the parameter space of η and ϵ . The red region corresponds to ϵ too large to form domain walls with scaling evolution. Grey region corresponds to the case where ϵ is small and domain walls dominate the energy density eventually. Here we have taken $\rho_1 = 0.4$ and $g_* = 134$.

where all the terms represent their scaled versions now.

A.2 Calculation of Gravitational Waves

Let us look at the theory of GWs in an expanding universe. We use the Green's method of [97, 98] in this section. We consider GWs to be sourced by tensor perturbations in the spatially flat FLRW metric,

$$ds^2 = -dt^2 + a^2(t) (\delta_{ij} + h_{ij}) dx^i dx^j \quad (\text{A.4})$$

where $a(t)$ is the scale factor, h_{ij} is the tensor perturbation satisfying the transverse-traceless (TT) condition $\partial_i h_{ij} = 0$ and which obeys the linearized Einstein equation,

$$\ddot{h}_{ij}(t, \mathbf{x}) + 3H\dot{h}_{ij}(t, \mathbf{x}) - \frac{\nabla^2}{a^2} h_{ij}(t, \mathbf{x}) = \frac{16\pi G}{a^2} T_{ij}^{\text{TT}}(t, \mathbf{x}) \quad (\text{A.5})$$

where dot denotes derivative with respect to cosmic time t and T^{TT} is the TT part of the energy-momentum tensor. Our treatment is valid for arbitrarily expanding universe with,

$$a(t) \propto \tau^\alpha \propto t^\gamma \quad (\text{A.6})$$

In the spatial Fourier space and in terms of conformal time $d\tau = dt/a(t)$, this equation takes the form,

$$h_{ij}''(t, \mathbf{k}) + \frac{2\alpha}{\tau} h_{ij}'(\tau, \mathbf{k}) + k^2 h_{ij}(\tau, \mathbf{k}) = 16\pi G T_{ij}^{\text{TT}}(\tau, \mathbf{k}) \quad (\text{A.7})$$

where prime notation denotes derivative with respect to conformal time. In terms of the rescaled metric,

$$\bar{h}_{ij} = ah_{ij} \quad (\text{A.8})$$

we obtain,

$$\left[\frac{\partial^2}{\partial x^2} + \left(1 - \frac{4\nu^2 - 1}{4x^2} \right) \right] \bar{h}_{ij}(\tau, \mathbf{k}) = \frac{16\pi G a(\tau)}{k^2} T_{ij}^{TT}(\tau, \mathbf{k}) \quad (\text{A.9})$$

where $x = k\tau$, and ν is defined as,

$$\nu = \alpha - \frac{1}{2} = \frac{3\gamma - 1}{2(1 - \gamma)} \quad (\text{A.10})$$

Our source T^{TT} is active in the interval $\tau_i < \tau < \tau_f$. The solution of Eq. (A.9) with initial condition $\bar{h}_{ij}(\tau_i) = \bar{h}'_{ij}(\tau_i) = 0$ can be found using Green's method (for $\tau \leq \tau_f$),

$$\bar{h}_{ij}(\tau, \mathbf{k}) = \frac{8\pi^2 G}{k^2} \int_{x_i}^x dy (yx)^{1/2} [N_\nu(x)J_\nu(y) - J_\nu(x)N_\nu(y)] a(y) T_{ij}^{TT}(y, \mathbf{k}) \quad (\text{A.11})$$

where $J_\nu(x)$ and $N_\nu(x)$ are the Bessel and Neumann functions. For $\nu = 1/2$, we get the solution for radiation dominated era.

When $\tau \geq \tau_f$, the source becomes negligible and the homogeneous solution to Eq. (A.9) is a linear combination of $J_\nu(x)$ and $N_\nu(x)$,

$$\bar{h}_{ij}(\tau, \mathbf{k}) = A_{ij}(\mathbf{k})(k\tau)^{1/2} J_\nu(k\tau) + B_{ij}(\mathbf{k})(k\tau)^{1/2} N_\nu(k\tau) \quad (\text{for } \tau \geq \tau_f) \quad (\text{A.12})$$

Coefficients $A_{ij}(\mathbf{k}), B_{ij}(\mathbf{k})$ can be found by equating Eq. (A.11) and (A.12) at $\tau = \tau_f$,

$$\begin{aligned} A_{ij}(\mathbf{k}) &= -\frac{8\pi^2 G}{k^2} \int_{x_i}^{x_f} dx \sqrt{x} a(x) N_\nu(x) T_{ij}^{TT}(x, \mathbf{k}) \\ B_{ij}(\mathbf{k}) &= \frac{8\pi^2 G}{k^2} \int_{x_i}^{x_f} dx \sqrt{x} a(x) J_\nu(x) T_{ij}^{TT}(x, \mathbf{k}) \end{aligned} \quad (\text{A.13})$$

Thus, if we can construct the $T^{TT}(x, \mathbf{k})$, we can calculate the perturbation $h_{ij}(\tau, \mathbf{k})$. The energy density of GWs is given by [99],

$$\begin{aligned} \rho_{\text{gw}} &= \frac{1}{32\pi G} \langle \dot{h}_{ij}(t, \mathbf{x}) \dot{h}_{ij}(t, \mathbf{x}) \rangle \\ &\simeq \frac{1}{32\pi G a^4(\tau)} \langle \bar{h}'_{ij}(\tau, \mathbf{x}) \bar{h}'_{ij}(\tau, \mathbf{x}) \rangle \end{aligned} \quad (\text{A.14})$$

where we have ignored higher order terms of aH for the second equality, since we assume that the wavelength of GWs is smaller than the Hubble radius, e.g. $k\tau \gg 1$.

A more useful quantity for observational cosmology is the fraction of energy density of GWs to the total energy density of the universe at time t , defined by,

$$\Omega_{gw}(t) = \frac{1}{\rho_c(t)} \frac{d\rho_{gw}(t)}{d \ln k} \quad (\text{A.15})$$

where $\rho_c(t)$ is the critical density of the universe at time t . Note the k is the magnitude of the *comoving wavevector*. It is related to the frequency observed at time t as,

$$f = \frac{k}{2\pi a(t)} \quad (\text{A.16})$$

where we set the scale factor at the initial time t_i to be unity, $a(t_i) = 1$.

A.2.1 Discretizing Equation of Motion

We follow the notation and method of discretization from [100]. We also modify the codes given in the reference to fit our requirements for the simulation. We start with the equation of motion in Eq. (A.3), with boundary conditions,

$$r(x, y, z, 0) = I(x, y, z) \quad (\text{A.17})$$

$$\frac{\partial}{\partial t} r(x, y, z, 0) = V(x, y, z) = 0 \quad (\text{A.18})$$

$$r(0, y, z, t) = r(L_x, y, z, t) \quad (\text{A.19})$$

$$r(x, 0, z, t) = r(x, L_y, z, t) \quad (\text{A.20})$$

$$r(x, y, 0, t) = r(x, y, L_z, t) \quad (\text{A.21})$$

where $I(x, y, z)$ is the prescribed initial condition. $L_x = L_y = L_z = b$ is the size of the comoving simulation box. The last three equations represent periodic boundary condition.

Our 3D mesh contains $N_x \times N_y \times N_z$ mesh points. We also subdivide the time domain $[t_{ini}, t_{fin} = T]$ into N_t discrete equidistant points $\{t_0 = T_i < t_1 < t_2 < \dots < T\}$. Now the field can be defined at each mesh point at a given time by the notation $r(x_i, y_j, z_k, t_n) = r_{ijk}^n$, where superscript n denotes time coordinate and subscripts i, j, k denote x, y, z coordinates respectively.

To discretize the wave equation, we replace the derivatives by central differences as follows,

$$\frac{\partial}{\partial t} r_{ijk}^n = [D_{2t}r]_{ijk}^n \approx \frac{r_{ijk}^{n+1} - r_{ijk}^{n-1}}{2\Delta t} \quad (\text{A.22})$$

$$\frac{\partial^2}{\partial t^2} r_{ijk}^n = [D_t D_t r]_{ijk}^n \approx \frac{r_{ijk}^{n+1} - 2r_{ijk}^n + r_{ijk}^{n-1}}{\Delta t^2} \quad (\text{A.23})$$

$$\frac{\partial^2}{\partial x^2} r_{ijk}^n = [D_x D_x r]_{ijk}^n \approx \frac{r_{i+1jk}^n - 2r_{ijk}^n + r_{i-1jk}^n}{\Delta x^2} \quad (\text{A.24})$$

and similarly for y and z coordinates. D_t, D_x represents the derivative operators in a compact notation. In this notation (omitting the space-time indices), Eq. (A.3) becomes,

$$D_t D_t r + 3H D_{2t} r - \frac{1}{a^2} [D_x D_x + D_y D_y + D_z D_z] r + \rho_1 r (r^2 - 1) + \epsilon (r^2 - 1) = 0 \quad (\text{A.25})$$

This, in discrete form can be written as,

$$\begin{aligned} & \frac{r_{ijk}^{n+1} - 2r_{ijk}^n + r_{ijk}^{n-1}}{\Delta t^2} + 3H^n \frac{r_{ijk}^{n+1} - 2r_{ijk}^n + r_{ijk}^{n-1}}{\Delta t^2} - \frac{1}{(a^n)^2} \left[\frac{r_{i+1jk}^n - 2r_{ijk}^n + r_{i-1jk}^n}{\Delta x^2} \right. \\ & \left. + \frac{r_{ij+1k}^n - 2r_{ijk}^n + r_{ij-1k}^n}{\Delta y^2} + \frac{r_{ijk+1}^n - 2r_{ijk}^n + r_{ijk-1}^n}{\Delta z^2} \right] + \rho_1 r_{ijk}^n ((r_{ijk}^n)^2 - 1) \\ & + \epsilon ((r_{ijk}^n)^2 - 1) = 0 \end{aligned} \quad (\text{A.26})$$

Provided we know the state r^n and r^{n-1} at time slices n and $n-1$, we can solve this algebraic equation for r^{n+1} ,

$$\begin{aligned} r_{ijk}^{n+1} = & \left(1 + \frac{3}{2}A^n\right)^{-1} \left[\{2 - \rho_1 \Delta t^2 ((r_{ijk}^n)^2 - 1)\} r_{ijk}^n + \epsilon \Delta t^2 ((r_{ijk}^n)^2 - 1) \right. \\ & \left. + \left(\frac{3}{2}A^n - 1\right) r_{ijk}^{n-1} + B_x^n \{r_{i+1jk}^n - 2r_{ijk}^n + r_{i-1jk}^n\} + B_y^n \{\dots\} + B_z^n \{\dots\} \right] \end{aligned} \quad (\text{A.27})$$

where $A^n = H^n \Delta t$, and $B_x^n = \frac{\Delta t^2}{(a^n)^2 \Delta x^2}$ and similarly for B_y^n, B_z^n .

Eq. (A.27) is not valid for $n=0$, which is the first time step in the simulation. We note that the initial velocity of the field is given by,

$$V_{ijk}^0 = \frac{r_{ijk}^1 - r_{ijk}^{-1}}{2\Delta t} \implies r_{ijk}^{-1} = r_{ijk}^1 - 2\Delta t V_{ijk}^0 \quad (\text{A.28})$$

Substituting this into Eq. (A.27), and solving for r_{ijk}^1 gives,

$$\begin{aligned} r_{ijk}^1 = & \frac{1}{2} \left[\left\{ 2 - \rho_1 \Delta t^2 (r_{ijk}^0)^2 - 1 \right\} r_{ijk}^0 + \epsilon \Delta t^2 (r_{ijk}^0)^2 - 1 \right] + \left(\frac{3}{2} A^0 - 1 \right) 2\Delta t V \\ & + B_x^0 \{\dots\} + B_y^0 \{\dots\} + B_z^0 \{\dots\} \end{aligned} \quad (\text{A.29})$$

Eq. (A.27) along with (A.29) represent the recursive relations that we will use in our simulation.

A.2.2 Periodic Boundary Condition:

Periodic boundary condition is implemented on the 6 sides of the simulation box. It is done to *mimic* the simulation over large distances and long times. The wave exiting through one side of the simulation box enters the box immediately through the opposite side, that way making the wave motion *periodic*. The strategy to implement periodic boundary condition is as follows: apply *open boundary condition* on side A of the box, and equate the opposite side B with A. That way, any displacement at side A will be instantly reflected at side B. And we have 3 such AB pairs.

Open boundary condition means a wave should be able to pass through the boundary without any resistance. In 3D, the condition we implement is [100],

$$D_t^+ r + c_x D_x^- r + c_y D_y^- r + c_z D_z^- r = 0 \Big|_{N_x, N_y, N_z}^n \quad (\text{A.30})$$

where D represents the derivative operators and the superscript \pm represents forward or backward finite difference. In our case, $c_x = c_y = c_z = \tilde{c} = 1/\sqrt{3}$ are wave velocities along x, y, z directions. This equation is implemented at all time (denoted by superscript n) at the 3 boundaries of the cube (denoted by subscript N_x, N_y, N_z). Solving for $r_{N_x, j, k}^{n+1}$ at N_x we get,

$$\begin{aligned} r_{N_x, j, k}^{n+1} = & r_{N_x, j, k}^n - \frac{\bar{C}_x}{\sqrt{3}} (r_{N_x, j, k}^n - r_{N_x-1, j, k}^n) - \frac{\bar{C}_y}{\sqrt{3}} (r_{N_x, j, k}^n - r_{N_x, j-1, k}^n) \\ & - \frac{\bar{C}_z}{\sqrt{3}} (r_{N_x, j, k}^n - r_{N_x, j, k-1}^n) \end{aligned} \quad (\text{A.31})$$

where $\bar{C}_{x,y,z} = \frac{\Delta t}{\Delta x, y, z}$ are the *Courant numbers*. We get similar recursive relations for r_{N_y/N_z}^{n+1} at N_y/N_z . We use these equations to update the N_x, N_y, N_z boundaries of the box while we equate the opposite sides, at $-N_x, -N_y, -N_z$ with them.

A.2.3 Stability Condition:

We can consider the coefficients B_x, B_y, B_z from Eq. (A.27) to be analogous to *Courant numbers* [100], and exert the stability condition for the simulation to be,

$$\max(B_x^n) + \max(B_y^n) + \max(B_z^n) \leq 1 \quad (\text{A.32})$$

As $B_x^n = \frac{\Delta t^2}{a^{n2} \Delta x^2}$, this gives,

$$\Delta t \leq \min(a^n) \left(\frac{1}{\Delta x^2} + \frac{1}{\Delta y^2} + \frac{1}{\Delta z^2} \right)^{-1/2} = \left(\frac{1}{\Delta x^2} + \frac{1}{\Delta y^2} + \frac{1}{\Delta z^2} \right)^{-1/2} \quad (\text{A.33})$$

Simulation Procedure

1. Define initial conditions as in Eq. (4.10) by discretizing it.
2. Perform first time step using Eq. (A.29).
3. Update the field using Eq. (A.27) in iteration for $n > 0$.

References

- [1] B. P. Abbott and et. al., *Observation of Gravitational Waves from a Binary Black Hole Merger*, *Phys. Rev. Lett.* **116** (2016), no. 6 61102.
- [2] A. Einstein, *Naherungsweise Integration der Feldgleichungen der Gravitation*, *Sitzungsberichte der Koniglich Preuischen Akademie der Wissenschaften (Berlin)* (1, 1916) 688–696.
- [3] C. Caprini and D. G. Figueroa, *Cosmological backgrounds of gravitational waves*, *Classical and Quantum Gravity* **35** (8, 2018) 163001.
- [4] B. P. Abbott and et. al., *Exploring the sensitivity of next generation gravitational wave detectors*, *Classical and Quantum Gravity* **34** (2, 2017) 044001.
- [5] P. R. Saulson, *Fundamentals of Interferometric Gravitational Wave Detectors*. World Scientific, 2nd. ed. ed., 2017.

- [6] A. N. Lommen, *Pulsar timing arrays: the promise of gravitational wave detection*, *Reports on Progress in Physics* **78** (12, 2015) 124901.
- [7] D. Chang, R. N. Mohapatra, and M. K. Parida, *Decoupling of Parity- and $SU(2)_R$ -Breaking Scales: A New Approach to Left-Right Symmetric Models*, *Physical Review Letters* **52** (3, 1984) 1072–1075.
- [8] D. Chang, R. N. Mohapatra, and M. K. Parida, *New approach to left-right-symmetry breaking in unified gauge theories*, *Physical Review D* **30** (9, 1984) 1052–1063.
- [9] K. S. Babu and A. Patra, *Higgs boson spectra in supersymmetric left-right models*, *Physical Review D* **93** (3, 2016) 055030.
- [10] L. Basso, B. Fuks, M. E. Krauss, and W. Porod, *Doubly-charged Higgs and vacuum stability in left-right supersymmetry*, *Journal of High Energy Physics* 2015 2015:7 **2015** (7, 2015) 1–25.
- [11] R. N. Mohapatra and J. C. Pati, *“Natural” left-right symmetry*, *Physical Review D* **11** (5, 1975) 2558–2561.
- [12] G. Senjanovic and R. N. Mohapatra, *Exact left-right symmetry and spontaneous violation of parity*, *Physical Review D* **12** (9, 1975) 1502–1505.
- [13] G. C. Branco and L. Lavoura, *Natural CP breaking in left-right symmetric theories*, *Physics Letters B* **165** (12, 1985) 327–332.
- [14] J. Basecq, J. Liu, J. Milutinovic, and L. Wolfenstein, *Spontaneous CP Violation in $SU(2)_l \times SU(2)_r \times U(1)-(B-l)$ Models*, *Nucl. Phys. B* **272** (1986) 145–157.
- [15] J. F. Gunion, J. Grifols, A. Mendez, B. Kayser, and F. Olness, *Higgs bosons in left-right-symmetric models*, *Physical Review D* **40** (9, 1989) 1546–1561.
- [16] G. Barenboim, M. Gorbahn, U. Nierste, and M. Raidal, *Higgs Sector of the Minimal Left-Right Symmetric Model*, *Phys. Rev. D* **65** (2002) 95003.
- [17] K. Kiers, M. Assis, and A. A. Petrov, *Higgs sector of the left-right model with explicit CP violation*, *Physical Review D* **71** (6, 2005) 115015.
- [18] J. Chakraborty, P. Konar, and T. Mondal, *Copositive criteria and boundedness of the scalar potential*, *Physical Review D* **89** (5, 2014) 095008.
- [19] B. Brahmachari, M. K. Samal, and U. Sarkar, *Potential Minimization in Left-Right Symmetric Models*, .
- [20] H. Fritzsch and P. Minkowski, *Unified interactions of leptons and hadrons*, *Annals of Physics* **93** (1975), no. 1 193–266.
- [21] H. Georgi, *The state of the art—gauge theories*, in *AIP Conference Proceedings*, vol. 23, pp. 575–582, American Institute of Physics, 1975.
- [22] C. Arbeláez, J. C. Romão, M. Hirsch, and M. Malinský, *LHC-scale left-right symmetry and unification*, *Physical Review D* **89** (2, 2014) 035002.
- [23] F. F. Deppisch, T. E. Gonzalo, and L. Graf, *Surveying the $SO(10)$ model landscape: The left-right symmetric case*, *Physical Review D* **96** (9, 2017) 055003.
- [24] N. T. Shaban and W. J. Stirling, *Minimal left-right symmetry and $SO(10)$ grand unification using LEP coupling constant measurements*, *Physics Letters B* **291** (9, 1992) 281–287.
- [25] C.-Y. Chen, P. S. B. Dev, and R. N. Mohapatra, *Probing heavy-light neutrino mixing in left-right seesaw models at the LHC*, *Physical Review D* **88** (8, 2013) 033014.

- [26] M. Lindner, F. S. Queiroz, W. Rodejohann, and C. E. Yaguna, *Left-right symmetry and lepton number violation at the Large Hadron electron Collider*, *Journal of High Energy Physics* **2016** (2016), no. 6 140.
- [27] S. Patra, F. S. Queiroz, and W. Rodejohann, *Stringent dilepton bounds on left-right models using LHC data*, *Physics Letters B* **752** (1, 2016) 186–190.
- [28] P. S. Dev, D. Kim, and R. N. Mohapatra, *Disambiguating seesaw models using invariant mass variables at hadron colliders*, *Journal of High Energy Physics 2016 2016:1* **2016** (1, 2016) 1–37.
- [29] Y. Rodríguez and C. Quimbay, *Spontaneous CP phases and flavour changing neutral currents in the left–right symmetric model*, *Nuclear Physics B* **637** (8, 2002) 219–242.
- [30] M. Nemevšek, F. Nesti, and G. Popara, *Keung-Senjanović process at the LHC: From lepton number violation to displaced vertices to invisible decays*, *Physical Review D* **97** (6, 2018) 115018.
- [31] P. S. Dev, R. N. Mohapatra, and Y. Zhang, *Probing the Higgs sector of the minimal Left-Right symmetric model at future hadron colliders*, *Journal of High Energy Physics 2016 2016:5* **2016** (5, 2016) 1–55.
- [32] A. Maiezza, M. Nemevšek, F. Nesti, and G. Senjanović, *Left-right symmetry at LHC*, *Physical Review D* **82** (9, 2010) 055022.
- [33] R. Rajaraman, *Solitons and instantons: An introduction to solitons and instantons in quantum field theory.*-North-Holland Publishing Company: Amsterdam, New York, Oxford, .
- [34] G. B. Gelmini, M. Gleiser, and E. W. Kolb, *Cosmology of biased discrete symmetry breaking*, *Physical Review D* **39** (3, 1989) 1558–1566.
- [35] Y. B. Zel’dovich, I. Y. Kobzarev, and L. B. Okun, *Cosmological consequences of spontaneous violation of discrete symmetry*, *Zh. Eksp. Teor. Fiz.* **40** (1974) 3–11.
- [36] B. Rai and G. Senjanović, *Gravity and the domain-wall problem*, *Physical Review D* **49** (3, 1994) 2729–2733.
- [37] A. Vilenkin, *Gravitational field of vacuum domain walls and strings*, *Physical Review D* **23** (2, 1981) 852–857.
- [38] P. Sikivie, *Axions, Domain Walls, and the Early Universe*, *Physical Review Letters* **48** (4, 1982) 1156–1159.
- [39] A. K. Mohanty and F. W. Stecker, *Matter-antimatter domains: A possible solution to the CP domain wall problem in the early universe*, *Physics Letters B* **143** (8, 1984) 351–356.
- [40] Z. Lalak, B. A. Ovrut, and S. Thomas, *Large-scale structure as a critical phenomenon*, *Physical Review D* **51** (5, 1995) 5456–5474.
- [41] D. Coulson, Z. Lalak, and B. Ovrut, *Biased domain walls*, *Physical Review D* **53** (4, 1996) 4237–4246.
- [42] J. M. Cline, U. A. Yajnik, S. N. Nayak, and M. Rabikumar, *Transient domain walls and lepton asymmetry in the left-right symmetric model*, *Phys. Rev. D* **66** (2002) 065001, [[hep-ph/0204319](#)].
- [43] A. Sarkar, Abhishek, and U. A. Yajnik, *PeV scale left-right symmetry and baryon asymmetry of the Universe*, *Nucl. Phys. B* **800** (2008) 253–269, [[arXiv:0710.5410](#)].
- [44] E. Witten, *Cosmic separation of phases*, *Physical Review D* **30** (7, 1984) 272–285.

- [45] C. J. Hogan, *Nucleation of cosmological phase transitions*, *Physics Letters B* **133** (1983), no. 3 172–176.
- [46] C. J. Hogan, *Gravitational radiation from cosmological phase transitions*, *Monthly Notices of the Royal Astronomical Society* **218** (2, 1986) 629–636.
- [47] M. S. Turner and F. Wilczek, *Relic gravitational waves and extended inflation*, *Physical Review Letters* **65** (12, 1990) 3080–3083.
- [48] M. Kamionkowski, A. Kosowsky, and M. S. Turner, *Gravitational radiation from first-order phase transitions*, *Physical Review D* **49** (3, 1994) 2837–2851.
- [49] C. Grojean and G. Servant, *Gravitational waves from phase transitions at the electroweak scale and beyond*, *Physical Review D* **75** (2, 2007) 043507.
- [50] J. Ellis, M. Lewicki, and J. M. No, *On the maximal strength of a first-order electroweak phase transition and its gravitational wave signal*, *Journal of Cosmology and Astroparticle Physics* **2019** (4, 2019) 003–003.
- [51] V. Brdar, L. Graf, A. J. Helmboldt, and X.-J. Xu, *Gravitational waves as a probe of left-right symmetry breaking*, *Journal of Cosmology and Astroparticle Physics* **2019** (12, 2019) 027–027.
- [52] M. Kawasaki and K. Saikawa, *Study of gravitational radiation from cosmic domain walls*, *Journal of Cosmology and Astroparticle Physics* **2011** (9, 2011) 008–008.
- [53] T. Hiramatsu, M. Kawasaki, and K. Saikawa, *On the estimation of gravitational wave spectrum from cosmic domain walls*, .
- [54] K. . Ichi Saikawa, *A Review of Gravitational Waves from Cosmic Domain Walls*, *Universe 2017, Vol. 3, Page 40* **3** (5, 2017) 40.
- [55] R. N. Mohapatra and J. C. Pati, *A Natural Left-Right Symmetry*, *Phys. Rev.* **D11** (1975) 2558.
- [56] J. C. Pati and A. Salam, *Lepton Number as the Fourth Color*, *Phys. Rev.* **D10** (1974) 275–289. [Erratum: *Phys. Rev.*D11,703(1975)].
- [57] G. Senjanovic and R. N. Mohapatra, *Exact Left-Right Symmetry and Spontaneous Violation of Parity*, *Phys.Rev.* **D12** (1975) 1502.
- [58] G. Senjanovic, *Spontaneous Breakdown of Parity in a Class of Gauge Theories*, *Nucl. Phys.* **B153** (1979) 334–364.
- [59] R. N. Mohapatra and G. Senjanovic, *Neutrino mass and spontaneous parity nonconservation*, *Phys. Rev. Lett.* **44** (1980) 912.
- [60] R. N. Mohapatra and G. Senjanovic, *Neutrino Masses and Mixings in Gauge Models with Spontaneous Parity Violation*, *Phys. Rev.* **D23** (1981) 165.
- [61] J. C. Pati and A. Salam, *Unified Lepton-Hadron Symmetry and a Gauge Theory of the Basic Interactions*, *Phys. Rev.* **D8** (1973) 1240–1251.
- [62] J. C. Pati and A. Salam, *Are There Anomalous Lepton-Hadron Interactions?*, *Phys. Rev. Lett.* **32** (1974) 1083.
- [63] N. G. Deshpande, J. F. Gunion, B. Kayser, and F. Olness, *Left-right-symmetric electroweak models with triplet Higgs field*, *Physical Review D* **44** (8, 1991) 837–858.
- [64] T. W. B. Kibble, *Topology of Cosmic Domains and Strings*, *J. Phys. A* **9** (1976) 1387–1398.

- [65] T. W. B. Kibble, *Some Implications of a Cosmological Phase Transition*, *Phys. Rept.* **67** (1980) 183.
- [66] J. W. Essam, *Percolation theory*, *Reports on Progress in Physics* **43** (7, 1980) 833–912.
- [67] D. Stauffer, *Scaling theory of percolation clusters*, *Physics Reports* **54** (7, 1979) 1–74.
- [68] T. Hiramatsu, M. Kawasaki, and K. Saikawa, *Gravitational waves from collapsing domain walls*, *Journal of Cosmology and Astroparticle Physics* **2010** (5, 2010) 032–032.
- [69] C. L. Wainwright, *CosmoTransitions: Computing cosmological phase transition temperatures and bubble profiles with multiple fields*, *Computer Physics Communications* **183** (9, 2012) 2006–2013.
- [70] K. Kadota, M. Kawasaki, and K. Saikawa, *Gravitational waves from domain walls in the next-to-minimal supersymmetric standard model*, *Journal of Cosmology and Astroparticle Physics* **2015** (10, 2015) 041–041.
- [71] T. Hiramatsu, M. Kawasaki, and K. Saikawa, *On the estimation of gravitational wave spectrum from cosmic domain walls*, *Journal of Cosmology and Astroparticle Physics* **2014** (2, 2014) 031–031.
- [72] A. Paul, U. Mukhopadhyay, and D. Majumdar, *Gravitational wave signatures from domain wall and strong first-order phase transitions in a two complex scalar extension of the Standard Model*, *Journal of High Energy Physics 2021 2021:5* **2021** (5, 2021) 1–28.
- [73] W. H. Press, B. S. Ryden, and D. N. Spergel, *Dynamical Evolution of Domain Walls in an Expanding Universe*, *Astrophys. J.* **347** (1989) 590–604.
- [74] D. Coulson, Z. Lalak, and B. A. Ovrut, *Biased domain walls*, *Phys. Rev. D* **53** (1996) 4237–4246.
- [75] T. Garagounis and M. Hindmarsh, *Scaling in numerical simulations of domain walls*, *Phys. Rev. D* **68** (2003) 103506, [[hep-ph/0212359](#)].
- [76] J. C. R. E. Oliveira, C. J. A. P. Martins, and P. P. Avelino, *The Cosmological evolution of domain wall networks*, *Phys. Rev. D* **71** (2005) 083509, [[hep-ph/0410356](#)].
- [77] P. P. Avelino, J. C. R. E. Oliveira, and C. J. A. P. Martins, *Understanding domain wall network evolution*, *Phys. Lett. B* **610** (2005) 1–8, [[hep-th/0503226](#)].
- [78] S. E. Larsson, S. Sarkar, and P. L. White, *Evading the cosmological domain wall problem*, *Phys. Rev. D* **55** (1997) 5129–5135, [[hep-ph/9608319](#)].
- [79] M. Hindmarsh, *Analytic scaling solutions for cosmic domain walls*, *Phys. Rev. Lett.* **77** (1996) 4495–4498, [[hep-ph/9605332](#)].
- [80] M. Hindmarsh, *Level set method for the evolution of defect and brane networks*, *Phys. Rev. D* **68** (2003) 043510, [[hep-ph/0207267](#)].
- [81] P. P. Avelino, C. J. A. P. Martins, and J. C. R. E. Oliveira, *One-scale model for domain wall network evolution*, *Phys. Rev. D* **72** (2005) 083506, [[hep-ph/0507272](#)].
- [82] M. Hindmarsh, S. J. Huber, K. Rummukainen, and D. J. Weir, *Gravitational Waves from the Sound of a First Order Phase Transition*, *Physical Review Letters* **112** (1, 2014) 041301.
- [83] S. Coleman, *Fate of the false vacuum: Semiclassical theory*, *Physical Review D* **15** (5, 1977) 2929–2936.

- [84] A. D. Linde, *Decay of the false vacuum at finite temperature*, *Nuclear Physics B* **216** (5, 1983) 421–445.
- [85] J. R. Espinosa, T. Konstandin, J. M. No, and G. Servant, *Energy budget of cosmological first-order phase transitions*, *Journal of Cosmology and Astroparticle Physics* **2010** (6, 2010) 028–028.
- [86] M. Li, Q.-S. Yan, Y. Zhang, and Z. Zhao, *Prospects of gravitational waves in the minimal left-right symmetric model*, *Journal of High Energy Physics* **2021** (2021), no. 3 267.
- [87] A. Kosowsky, M. S. Turner, and R. Watkins, *Gravitational radiation from colliding vacuum bubbles*, *Physical Review D* **45** (6, 1992) 4514–4535.
- [88] C. Caprini and R. Durrer, *Gravitational waves from stochastic relativistic sources: Primordial turbulence and magnetic fields*, *Physical Review D* **74** (9, 2006) 063521.
- [89] A. Kosowsky and M. S. Turner, *Gravitational radiation from colliding vacuum bubbles: Envelope approximation to many-bubble collisions*, *Physical Review D* **47** (5, 1993) 4372–4391.
- [90] S. J. Huber and T. Konstandin, *Gravitational wave production by collisions: more bubbles*, *Journal of Cosmology and Astroparticle Physics* **2008** (9, 2008) 022.
- [91] D. J. Weir, *Revisiting the envelope approximation: Gravitational waves from bubble collisions*, *Physical Review D* **93** (6, 2016) 124037.
- [92] M. Hindmarsh, S. J. Huber, K. Rummukainen, and D. J. Weir, *Numerical simulations of acoustically generated gravitational waves at a first order phase transition*, *Physical Review D* **92** (12, 2015) 123009.
- [93] C. Caprini, M. Hindmarsh, S. Huber, T. Konstandin, J. Kozaczuk, G. Nardini, J. M. No, A. Petiteau, P. Schwaller, G. Servant, and D. J. Weir, *Science with the space-based interferometer eLISA. II: gravitational waves from cosmological phase transitions*, *Journal of Cosmology and Astroparticle Physics* **2016** (4, 2016) 001–001.
- [94] C. Caprini, R. Durrer, and G. Servant, *The stochastic gravitational wave background from turbulence and magnetic fields generated by a first-order phase transition*, *Journal of Cosmology and Astroparticle Physics* **2009** (12, 2009) 024–024.
- [95] P. Binétruy, A. Bohé, C. Caprini, and J.-F. Dufaux, *Cosmological backgrounds of gravitational waves and eLISA/NGO: phase transitions, cosmic strings and other sources*, *Journal of Cosmology and Astroparticle Physics* **2012** (6, 2012) 027–027.
- [96] K. Schmitz, *New Sensitivity Curves for Gravitational-Wave Signals from Cosmological Phase Transitions*, .
- [97] D. Stauffer, *Scaling theory of percolation clusters*, *Phys. Rept.* **54** (1979) 1–74.
- [98] J.-F. Dufaux, G. Felder, L. Kofman, and O. Navros, *Gravity Waves from Tachyonic Preheating after Hybrid Inflation*, *JCAP* **03** (2009) 001, [[arXiv:0812.2917](https://arxiv.org/abs/0812.2917)].
- [99] M. Maggiore, *Gravitational waves: Volume 1: Theory and experiments*, vol. 1. Oxford university press, 2008.
- [100] H. P. Langtangen, *Finite difference methods for wave motion*, *Department of Informatics, University of Oslo, preliminary version edition* (2016).